Expression of neuronal Na+ leak channel, NALCN, provides for persistent invasion of metastasizing cancer cells

Oksana Iamshanova[1,16], Dmitri Gordienko[1,16], Antoine Folcher[1,16], Alexandre Bokhobza[1], George Shapovalov[1], Dheeraj Kannancheri-Puthooru[1], Pascal Mariot[1], Laurent Allant[1], Emilie Desruelles[1], Corentin Spriet[2], Raquel Diez[3], Thibauld Oullier[4], Séverine Marionneau-Lambot[4], Lucie Brisson[5], Sandra Geraci[6], Hathaichanok Impheng[7], V'yacheslav Lehenkyi[1], Aurelien Haustrate[1], Adriana Mihalache[8], Pierre Gosset[8], Stéphanie Chadet[9], Stéphanie Retif[10], Maryline Laube[10], Julien Sobilo[10], Stéphanie Lerondel[10], Giulia Villari[11,12], Guido Serini[11,12], Alessandra Fiorio Pla[13], Sébastien Roger[9], Gaelle Fromont-Hankard[5,14], Mustafa Djamgoz[15], Philippe Clezardin[6], Arnaud Monteil[7], Natalia Prevarskaya[1,17,*]

[1]Inserm U1003, Laboratory of Excellence, Ion Channels Science and Therapeutics, Equipe Labellisée par la Ligue Nationale Contre le Cancer, SIRIC ONCOLille, University of Lille, 59656 Villeneuve d'Ascq, France

[2]TISBio, Unité de Glycobiologie Structurale et Fonctionnelle (UGSF), CNRS, UMR 8576, Université de Lille, 59000 Lille, France

[3]Cell Physiology Research Group, Department of Physiology, University of Extremadura, Cáceres, Spain.

[4]Cancéropôle du Grand Ouest, Plateforme In Vivo, 44000 Nantes, France

[5]Inserm UMR1069, Nutrition Croissance et Cancer, University of Tours, 10 boulevard Tonnellé, 37032 Tours, France.

[6]Univ Lyon, Université Claude Bernard Lyon 1, Inserm UMR 1033 LYOS, 69008 Lyon, France.

[7]IGF, CNRS, INSERM, University of Montpellier, LabEx 'Ion Channel Science and Therapeutics', Montpellier, France.

[8]Service d'Anatomie et de Cytologie Pathologiques, Groupement des Hôpitaux de l'Université Catholique de Lille, Lille, France.

[9]EA4245 Transplantation, Immunology, Inflammation, University of Tours, 10 boulevard Tonnellé, 37032 Tours, France

[10]PHENOMIN-TAAM, CNRS UPS44, Centre d'Imagerie du Petit Animal (CIPA), 3B rue de la Férollerie, 45071 Orléans cedex 2, France

[11] Department of Oncology, University of Torino School of Medicine, Candiolo (TO), Italy

[12] Candiolo Cancer Institute - Fondazione del Piemonte per l'Oncologia (FPO) Istituto di Ricovero e Cura a Carattere Scientifico (IRCCS), Candiolo (TO), Italy

[13] Department of Life Science and Systems Biology; University of Torino, 10126 Torino, Italy.

[14]CHRU de Tours, Department of Pathology, 2 Boulevard Tonnellé, 37000 Tours, France

[15]Neuroscience Solution to Cancer Research Group, Department of Life Sciences, Faculty of Natural Sciences, Sir Alexander Fleming Building, Imperial College London, South Kensington Campus, London SW7 2AZ, UK.

[16]These authors contributed equally

[17]Lead contact

[*]Correspondence: natacha.prevarskaya@univ-lille.fr

Keywords: Sodium leak channel, calcium oscillations, Src kinase, vesicle secretion, invasion, metastasis, oncochannelopathy.

Abstract

Cytosolic Ca2+ oscillations provide signaling input to several effector systems of the cell. These include neuronal development, migration and networking. Although similar signaling events are hijacked by highly aggressive cancer cells, the complexity of the 'neuron-like' remodeling in metastasis remains to be explored. Here, using a variety of in vitro and in vivo techniques we show that strongly metastatic prostate cancer cells acquire specific Na+/Ca2+ signature required for persistent invasion. We identify the 'neuronal' Na+ leak channel, NALCN, at the hot spots of the Ca2+ wave initiation and invadopodia formation. Mechanistically, NALCN associates functionally with plasmalemmal and mitochondrial Na+/Ca2+ exchangers, reactive oxygen species and store-operated channels to generate intracellular Ca2+ oscillations. In turn, this stimulates the activity of protooncogene Src kinase co-localized with NALCN, actin remodeling and secretion of proteolytic enzymes, thus increasing an invasive potential of the cancer cells and metastatic lesions in vivo (accessed in pre-clinical models). Overall, our findings provide new insight into the signaling pathway specific for metastatic cells where NALCN plays the role of the persistent invasion "launcher and controller".

Introduction

54 Prostate cancer (PCa) is the most common noncutaneous human malignancy and the second most lethal tumor
55 among men, with its highest incidence in industrialized countries. Understanding the processes facilitating the
56 progression of PCa to aggressive metastatic phenotypes and developing new therapeutic targets are necessary
57 to improve both the survival rate and the everyday life of the patients. In most cases of PCa, metastasis but not
58 the primary tumor *per se* is the main cause of mortality, with the bone metastases being the most likely and
59 highly incurable complication.
60 To effectively escape the tumor, enter the circulation and establish secondary growth in distant organs cancer
61 cells must develop an enhanced migration propensity. The invasion capacity gained by tumor cells is the
62 hallmark of malignancy. To become invasive, tumor cells need to acquire traits enabling enhanced migration
63 and proteolysis of extracellular matrix (ECM). There is increasing evidence indicating that development of
64 invasive tumor phenotype involves altered ionic homeostasis driven by aberrant ion channel
65 expression/function, referred to as 'oncochannelopathies' (Prevarskaya *et al*, 2018a). It is now well established
66 that, on the one hand, Ca^{2+} signaling plays a crucial role in cancer development (Monteith *et al*, 2017), while,
67 on the other hand, elevated tissue Na^{+} concentration is a highly specific *in vivo* indicator of malignant lesions in
68 human cancer patients (Haneder *et al*, 2015; Zaric *et al*, 2016). This pinpoints the unraveling of the mechanisms
69 coupling the alteration in Na^{+} homeostasis to intracellular Ca^{2+} events upon cancer progression as one of the
70 central subjects in the field of oncochannelopathies.
71 Over the years, several studies have revealed some striking similarities in the behavior between neuronal and
72 metastatic cancer cells. Indeed, gene products traditionally known for their role in normal neuronal migration,
73 axonal growth and embryonic development, were also pinpointed in metastasis, where they contribute to the
74 aggressive cancer phenotype (Shah *et al*, 2018; Biankin *et al*, 2012). Interestingly, ion channels responsible for
75 generation of action potential in the electrically excitable cells were also reported in metastatic cells (Djamgoz
76 *et al*, 2019). An intriguing player of neuron-like pathway in metastatic cancer cells seems to be the Na^{+} leak
77 channel, NALCN, first reported in neurons (Lu *et al*, 2007), and whose expression was then found to be altered
78 in some types of cancer (reviewed in (Cochet-Bissuel *et al*, 2014)) with, as yet, unknown consequences for
79 cancer cells behavior. NALCN baseline activity in neurons produces about 10 mV depolarizing shift in their
80 resting membrane potential (V_r) (Lu *et al*, 2007). However, most importantly, NALCN is part of a channelosome,
81 a multi-protein complex whose members are involved in channel folding, stabilization, cellular localization and
82 activation (Cochet-Bissuel *et al*, 2014) thereby providing great degree of versatility for the regulation of its
83 function not only in neurons, but also in cancer cells.

84 Another important question is how transmembrane Na^+ fluxes can promote cancer cell invasiveness.
85 Indeed, it is mainly dysregulated intracellular Ca^{2+} signaling, with the specific spatial and temporal signatures
86 adopted by cancer cells, which is currently acknowledged to drive the progression of certain cancer hallmarks,
87 including invasion and metastasizing (Prevarskaya *et al*, 2018b, 2011). Given the existence of several tightly
88 linked Na^+/Ca^{2+}-dependent molecular pathways that participate in the maintenance of the intracellular Ca^{2+} and
89 Na^+ homeostasis (Verkhratsky *et al*, 2018), we hypothesized that in metastatic cancer cells, NALCN could
90 provide signaling input encouraging the cell invasion via intracellular Ca^{2+} events.
91 Thus, in the present work we have undertaken a thorough investigation of the neuronal-type NALCN in
92 prostate cancer cells in the context of its significance for prostate carcinogenesis. Our findings identify NALCN
93 as a major mechanism responsible for Na^+ influx that governs Ca^{2+} oscillatory signaling (involving cytoplasm,
94 endoplasmic reticulum and mitochondria), ROS production and initiation of invadopodia formation (referred
95 hereafter as invadopodogenesis) in strongly metastatic prostate cancer cells. Importantly, formation of dynamin
96 puncta, reporting invadopodial precursor assembly, occurred at sites of the $[Ca^{2+}]_c$ wave initiation enriched with
97 NALCN. The NALCN-governed oscillatory Ca^{2+} events facilitate secretion of proteolytic enzymes (matrix
98 metalloproteinases, MMPs) and promote invadopodogenesis via Src kinase activation and actin remodeling
99 (also encouraged by N-WASP – Cdc42 coupling). Modulation of NALCN bioavailability strongly affects *in vivo*
100 prostate cancer progression and bone metastasis formation.
101 Overall, our study uncovers malignant assignment of NALCN and demonstrates its role as the central
102 element of critical Na^+/Ca^{2+} signaling axis promoting metastatic progression. Our data suggest that *NALCN*
103 gene must be included in the panel of screened genes for early diagnosis of metastatic prostate cancer.
104
105 **Results**
106 **NALCN promotes metastasis-associated cancer cell behavior**
107 Initial immunohistochemical analysis of human prostate tissue arrays detected NALCN upregulation
108 during cancer progression whereas NALCN was not detected in non-cancerous prostate glands (Figure 1a). In
109 clinically localized prostate cancer, NALCN expression was significantly higher within the ISUP group (Gleason
110 score that reflects loss of differentiation) (Table S1). NALCN expression was also significantly higher in pT3
111 tumors (with extra-prostatic extension) as compared to pT2 tumors (limited to the prostate gland) (Table S1). In
112 human prostate cancer, NALCN immunostaining was observed in 57% of clinically localized hormone-naïve
113 cases, 6% (3/48) of castration-resistant prostate cancer (CRPC) and 62% (13/21) of metastases. The

114 expression of NALCN was strongly correlated with the expression of Src-kinase (Figure 1b). *NALCN* mRNA
115 level was significantly higher in prostate cancer biopsies relative to non-cancerous tissues taken from the same
116 patients (Figure 1c). Similar results were obtained for NALCN expression in other cancers: positive staining in
117 bone metastases from breast (11/19) and colon (5/8) cancers, without any detectable expression in
118 corresponding normal tissues (0/5) (Figure 1d). These data suggest that NALCN expression has clinical
119 relevance and that NALCN may contribute to malignancy in several carcinomas.

120 Consistent with this, screening of various prostate cancer cell lines revealed NALCN and all members of
121 the NALCN channelosome - UNC-79, UNC-80 and NLF-1 - only in highly aggressive cell lines, with little or no
122 expression in weakly metastatic cells (Figures 1e and S1a). Furthermore, NALCN was functionally expressed
123 in the plasma membrane (PM) (Figure S1b), thus providing a pathway for Na^+ influx, which was not observed
124 in NALCN-negative cell lines (Figures S1c-e). Importantly, NALCN silencing did not affect cellular viability, cell
125 cycle progression, apoptosis (basal or induced) or proliferation (Figure S2), whereas metastasis-associated
126 behaviors (cellular motility, migration and invasion) were significantly dependent on the level of NALCN
127 expression (Figure 1f).

128 Recruitment of NALCN to invadopodogenesis was studied by cyanine-3 (Cy3)-fluorescent gelatinase
129 assay. NALCN silencing significantly suppressed the number of the invadopodium formation sites and the total
130 area of gelatin degradation (Figures 2a and S2f).

131 Previously, pro-invasive role of Na^+ influx through the de novo expressed Na_v channels in breast cancer
132 cells was ascribed to facilitated H^+ extrusion via Na^+/H^+ exchanger type 1 (NHE-1), leading to acidification of
133 the pericellular microenvironment and activation of ECM-degrading cysteine cathepsins at invadopodia sites
134 (Gillet *et al*, 2009a; Brisson *et al*, 2013a). Surprisingly, in our experiments, knockdown of Na^+-conducting
135 NALCN (NALCN-KD) had no effect on either intracellular pH or H^+ extrusion from the PC-3 cells (Figure S2g).
136 This argued against the possibility that metastasis-promoting significance of NALCN-mediated Na^+ influx in
137 prostate cancer cells is somehow linked to pH changes.

138 Immunocytochemical analysis revealed strong co-localization of NALCN with Src kinase, a key signaling
139 component of the invasion pathway, and with invadopodial proteins (cortactin, dynamin, matrix
140 metalloproteinase MT1-MMP and adaptor protein Tks5) within specific morphological structures referred to as
141 'invadopodia puncta and rosettes' (Figures 2b and S2q). At the same time, when PC-3 cells co-expressing
142 NALCN-GFP and Tks5 were placed on gelatin, it was newly formed invadopodia demonstrating the
143 colocalization of NALCN and Tks5 (Figure S3). NALCN targeting to invadopodia was also demonstrated by

144 subcellular fractionation (Figure S2p). Although previous studies have reported that Src kinase is recruited to
145 the NALCN channelosome (Lu *et al*, 2009), no evidence of direct Src kinase-dependence of NALCN expression
146 was presented. We have found that NALCN-KD markedly suppressed both Src kinase expression and activity
147 in metastatic PC-3 cells (Figures S2n and S2o).

148 Fetal bovine serum (FBS) containing the mixture of various growth factors, or epidermal growth factor
149 alone (EGF) which acts through surface receptor tyrosine kinases (RTKs) or G-protein-coupled receptors
150 (GPCRs) could be used to stimulate pro-invasive behavior of prostate cancer cells cultured under starving
151 conditions. Indeed, both FBS and EGF were reported as potent pro-invasive stimuli (Sun *et al*, 2014). It was
152 previously demonstrated that stimulation of starved melanoma cells with fetal bovine serum (FBS) induces Ca^{2+}
153 oscillations and facilitates invasion. However, the casual link between the two processes remained unknown.
154 We have found that in PC-3 cells, FBS also induced $[Ca^{2+}]_c$ response, associated with deviation of $PI(4,5)P_2$
155 (phosphatidylinositol 4,5-bisphosphate) from equilibrium, facilitated interaction between N-WASP (neuronal
156 Wiskott–Aldrich syndrome protein) and Cdc42 (cell division cycle 42 protein), and induced invadopodial
157 precursor assembly detectable as enriched F-actin and dynamin puncta (Figure S4). Importantly, this process
158 was strongly suppressed by NALCN-KD (Figure 2c). Consistent with our hypothesis of the existence in invasive
159 cells of a specific Ca^{2+}-Na^{+} signaling axis, we have found that formation of dynamin puncta, reporting
160 invadopodial precursor assembly in PC-3 cells, occurred at sites of $[Ca^{2+}]_c$ wave initiation (Figure 2d) that, in
161 turn, coincided with NALCN-enriched rosettes (Figure 2e).

162 **NALCN Drives Ca^{2+} Oscillations**

163 We have found that exposure of PC-3 cells to FBS or EGF alone induces an initial $[Ca^{2+}]_c$ transient
164 followed by $[Ca^{2+}]_c$ oscillations with reciprocal changes of Ca^{2+} concentration in the endoplasmic reticulum
165 ($[Ca^{2+}]_{ER}$) (Figures 3a and 3b). The initial $[Ca^{2+}]_c$ transient, but not the subsequent $[Ca^{2+}]_c$ oscillations, persisted
166 in Ca^{2+}-free solution supplemented with 0.5 mM EGTA, while both were abolished following Ca^{2+} store depletion
167 with 50 μM cyclopiazonic acid (CPA) even when the cells were bathed in Ca^{2+}-containing solution (Figure 3c).
168 We concluded, therefore, that generation of these $[Ca^{2+}]_c$ oscillations involves both Ca^{2+} entry and Ca^{2+} recycling
169 by the endoplasmic reticulum (ER).

170 To assess the role of NALCN in the $[Ca^{2+}]_c$ oscillations, we compared spatiotemporal patterns of the FBS-
171 induced $[Ca^{2+}]_c$ response in serum-starved control and NALCN-KD PC-3 cells (Figures 3d and 3e). This
172 revealed that the FBS-induced $[Ca^{2+}]_c$ oscillations (both frequency and signal temporal density) were
173 significantly attenuated in NALCN-KD cells (Figure 3f). Also, the Ca^{2+} "pacemaker phase" (i.e., the phase of

174 slow $[Ca^{2+}]_c$ rise preceding regenerative response) observed in these oscillations appeared NALCN-dependent
175 as well (Figures 3d and 3e). The $[Ca^{2+}]_c$ oscillations were attenuated dramatically by reducing extracellular Na^+
176 concentration ($[Na^+]_o$) (Figure 3g). Furthermore, application of FBS to PC-3 cells activated an oscillating inward
177 current. This current was dramatically reduced while oscillations were virtually completely abolished following
178 NALCN-KD or $[Na^+]_o$ omission (Figure 3h). These findings were substantiated by a reversal strategy: NALCN
179 overexpression (Figure S5) significantly increased FBS-induced inward current and the $[Ca^{2+}]_c$ oscillations
180 (Figures S5c-f).

181 Thus, exposure of serum-starved strongly metastatic PC-3 prostate cancer cells to FBS activates
182 NALCN-mediated Na^+ influx which appears to be causally linked to generation of $[Ca^{2+}]_c$ oscillations. Since PC-
183 3 cells exposure to FBS also enhanced Src kinase activity (Figure S6a), one can conclude that FBS-activated
184 NALCN-mediated Na^+ influx and ensuing oscillatory Ca^{2+} signaling (Figures 3) promote the activity of Src kinase
185 which transduces signals related to cellular proliferation, differentiation, motility and adhesion.

186 **Coupling between NALCN-mediated Na^+ influx and $[Ca^{2+}]_c$ events**

187 Oscillations generally require positive feedback between the contributing elements. We, therefore,
188 assessed (i) modulation of NALCN-mediated Na^+ influx by extracellular ($[Ca^{2+}]_o$) and intracellular ($[Ca^{2+}]_c$) Ca^{2+}
189 concentrations as well as (ii) coupling between Na^+ influx and rise of $[Ca^{2+}]_c$.

190 To unravel the net effect of $[Ca^{2+}]_c$ elevation on NALCN-mediated Na^+ influx, we assessed the Na^+ influx
191 induced by switching $[Na^+]_o$ from 0 to 130 mM (Figure 4a) and by store-operated Ca^{2+} entry (SOCE) (Figure 4c).
192 The two were then compared (Figure 4d, top). We have found that $[Na^+]_o$ rise induced a significant Na^+ influx
193 (Figure 4a, left) which: (i) was dramatically suppressed by NALCN-KD (see also Figure 4d); (ii) was not
194 modulated by $[Ca^{2+}]_o$, at least within the range of 0 – 4 mM (Figure 4a, middle; Figure S6c), in contrast to what
195 was reported for neurons (Lu *et al*, 2010); and (iii) was not affected by Ca^{2+} store depletion (Figure 4a right,
196 Figure S6d). Furthermore, $[Ca^{2+}]_c$ elevation brought about by acute inhibition of sarco/endoplasmic reticulum
197 Ca^{2+}-ATPase (SERCA) with thapsigargin (TG) failed to induce Na^+ influx when the cells were bathed in Ca^{2+}-
198 free external solution supplemented with 0.5 mM EGTA,
199 i.e., when SOCE was prevented (Figure 4b). Moreover, we have found (Figure 4c) that: (i) SOCE activation
200 triggers Na^+ influx even at constant physiological $[Na^+]_o$ in a $[Ca^{2+}]_o$-dependent manner (see also Figures S6c-
201 f); (ii) NALCN-KD significantly suppresses not only this Na^+ influx but also SOCE; and (iii) inhibition of the
202 reverse-mode of plasmalemmal Na^+/Ca^{2+} exchanger (RM-NCX) curtails $[Ca^{2+}]_c$ transient caused by SOCE at
203 $[Na^+]_o$=130 mM, does not affect it at $[Na^+]_o$=0 mM and attenuates $[Ca^{2+}]_c$ transient triggered by Na^+ readmission

204 following SOCE activation. Comparison of the effects of NALCN-KD on Na^+ influx caused by the $[Na^+]_o$ rise with
205 that triggered by SOCE revealed that SOCE significantly augmented NALCN-mediated Na^+ influx (Figure 4d,
206 top). In addition, the cell-surface biotinylation assay reported that SOCE increased expression of NALCN protein
207 in the PM (Figure 4d, bottom), similar to FBS (Figure S6g).

208 The above results indicate that Ca^{2+} influx during SOCE (Figures 4c,d), but not Ca^{2+} release from the ER
209 (Figure 4b) or Ca^{2+} store depletion *per se* (Figure 4a, right), enhances NALCN-mediated Na^+ influx by promoting
210 translocation of NALCN protein to the PM. In turn, the rise in cytosolic Na^+ concentration ($[Na^+]_c$) facilitates Ca^{2+}
211 influx either via reverse mode of plasma membrane Na^+/Ca^{2+} exchanger, RM-NCX (Figures 4c, middle; Figure
212 S6h), and/or by relieving SOCE inactivation. The latter may involve mitochondrial Na^+/Ca^{2+} exchanger (NCLX),
213 which was shown previously to affect SOCE via modulation of reactive oxygen species (ROS) production (Ben-
214 Kasus Nissim *et al*, 2017). Consistent with this, we have found that NCLX silencing indeed suppressed SOCE
215 (Figures 4c, right, and S6i).

216 Thus, in view of the obtained results the following sequence of events in PC-3 cells can be proposed:
217 NALCN-mediated Na^+ influx → NCLX-mediated Ca^{2+} extrusion from mitochondria → decrease of ROS
218 production → relief of SOCE inactivation. At the same time, attenuation of the FBS-induced $[Ca^{2+}]_c$ events (both
219 the initial transient and oscillations) by the RM-NCX inhibitor KB-R7943 (Figure 4e), suggests that NALCN-
220 mediated Na^+ influx facilitates RM-NCX-mediated Ca^{2+} entry, while inhibition of FBS-induced inward current by
221 this compound (Figure 4f) indicates that this Ca^{2+} entry encourages NALCN-mediated Na^+ influx. This positive
222 feedback between NALCN and RM-NCX is most likely the mechanism sustaining the $[Ca^{2+}]_c$ oscillations. The
223 modulation of the feedback via the ER Ca^{2+} recycling is also tuned by SOCE and RM-NCX (Figure 3a). We also
224 verified that the Na^+ influx, attributed to the NALCN-mediated current in PC-3 cells, is tetrodotoxin-resistant and
225 gadolinium-sensitive (Figures S6j-o), similar to neuronal NALCN (Lu *et al*, 2007).

226 **NALCN – NCLX functional coupling recruits mitochondria to regulation of $[Ca^{2+}]_c$ oscillations**

227 The tight functional coupling between SOCE and NALCN (Figures 4c,d), the dependence of $[Ca^{2+}]_c$
228 oscillations on NALCN-mediated Na^+ influx (Figures 3d-g) and the involvement of NCLX in SOCE regulation
229 (Figure 4c, right) via ROS-mediated oxidation of Ca^{2+} release-activated Ca^{2+} channel protein 1, Orai1 (Ben-
230 Kasus Nissim *et al*, 2017), suggest that, apart from RM-NCX, the NALCN-mediated Na^+ influx may also regulate
231 $[Ca^{2+}]_c$ oscillations via NCLX. Indeed, NCLX would exchange mitochondrial Ca^{2+} to Na^+ delivered via NALCN,
232 and hence oppose Ca^{2+} uptake by the mitochondrial Ca^{2+} uniporter (MCU) and subsequent ROS production.

233 Consistent with this, we observed that the FBS-induced $[Ca^{2+}]_c$ oscillations were associated with oscillations of
234 (i) Ca^{2+} concentration in mitochondria ($[Ca^{2+}]_{mito}$; Figure 5a) and (ii) mitochondrial superoxide ($O_2^{\cdot -}$) production
235 (Figure 5b). Also, application of H_2O_2 (endogenous product of $O_2^{\cdot -}$) suppressed the $[Ca^{2+}]_c$ oscillations (Figure
236 5c) .

237 In support of the above hypothesis, we have also found that NCLX silencing (siNCLX, S2T) dramatically
238 attenuated the FBS-induced $[Ca^{2+}]_c$ oscillations (Figure 5d). Interestingly, the initial $[Ca^{2+}]_c$ transient caused by
239 the FBS application had significantly longer duration in cells pre-treated with siNCLX, likely due to suppression
240 of SERCA by enhanced ROS production in mitochondria lacking NCLX (Qin *et al*, 2014). Thus, interplay
241 between Ca^{2+} and Na^+ signals not only would affect mitochondrial Ca^{2+} shuttling and mitochondrial redox status
242 (Ben-Kasus Nissim *et al*, 2017), but also serve to maintain persistent $[Ca^{2+}]_c$ oscillations. In turn, the latter are
243 necessary for Src activation (Sun *et al*, 2014).

244 **NALCN regulates secretion of ECM-degrading enzymes in Ca^{2+}-dependent manner**

245 In cancer cells, secretion of ECM-degrading enzymes is the principal mechanism facilitating
246 extracellular proteolysis and invasion (Friedl & Wolf, 2008). To assess a role of NALCN in regulation of secretion
247 in aggressive prostate cancer cells we have analyzed the effect of NALCN bioavailability on the rate of FBS-
248 induced secretion visualized by dynamic 3D confocal imaging (Figure 6a) of FM1-43 fluorescent reporter pre-
249 accumulated in the secretory vesicles of starved PC-3 cells. We have found that presence of NALCN proved to
250 be critical for controlling both the rate of vesicle secretion by PC-3 cells (Figures 6b,c) and the activity of ECM-
251 degrading enzymes (Figure 6d). Furthermore, by comparison of the effect of Ca^{2+} chelators with different
252 dynamic properties on the rate of this secretion, we have demonstrated that this process is not only Ca^{2+}-
253 dependent, but is, in fact, regulated by $[Ca^{2+}]_c$ in microdomains, since both fast and slow Ca^{2+} chelators
254 decreased the rate of secretion to different extents (Figures 6e,f).

255 **NALCN promotes prostate cancer aggressiveness *In Vivo***

256 Finally, we have analyzed the role of NALCN in cancer progression *in vivo* by using several mice models.
257 Since phosphatase and tensin homologue (PTEN) is one of the most commonly deleted/mutated tumor
258 suppressor genes in human prostate cancer, we utilized the PTEN-knockout mouse with conditional gene
259 inactivation (floxed allele; L2) as our first *in vivo* model (Parisotto *et al*, 2018). Following prolonged treatment
260 with tamoxifen, $PTEN^{-/-}$ mice produced prostate adenocarcinoma, whereas $PTEN^{-/-}p53^{-/-}$ developed more
261 aggressive and invasive phenotype of prostate cancer. *Ex vivo* analyses performed on these prostate tumors

262 revealed that NALCN was markedly upregulated in PTEN$^{-/-}$p53$^{-/-}$ tumors (i.e., during progression of invasive
263 adenocarcinoma), compared with the PTEN$^{-/-}$ tumors (i.e., during initial tumorigenesis) (Figure 7a).
264 For studying the progression of prostate tumors *in vivo*, we developed xenografts of PC-3 cells with stable
265 luciferase activity. Therefore, our second *in vivo* model was presented by the nude mice that were injected
266 orthotopically with these cells and followed for 12 weeks, allowing primary tumor growth and metastases
267 development. We found that using NALCN-KD PC-3 cells resulted in significantly suppressed metastasis and
268 primary tumor growth *in vivo* (Figures 7b-d). This was confirmed further by *ex vivo* analyses (Figure 7e). It is
269 well known that prostate cancer frequently metastasizes to bone (in fact, the PC-3 cell line was originally derived
270 from the bone metastases of a prostate cancer patient). We observed that injection of NALCN-KD PC-3 cells
271 caused significantly less skeletal metastases compared to the wild-type cells (Figure 7f). NALCN-KD also
272 induced a reduction of metastasis to other organs, albeit to a lesser extent (Figure 7e).
273
274 The above observations supported our hypothesis that NALCN expression determines metastatic
275 potential of PC-3 cells, specifically to the bone. Indeed, Transwell® invasion assay utilizing osteoblast
276 conditioned media as a chemoattractant showed significant reduction of the invasiveness of PC-3 cells with
277 NALCN-KD (Figure 7g). Furthermore, the direct injection of PC-3 cells into tibia of nude mice (third *in vivo*
278 model) revealed that the cells with NALCN-KD produced significantly less bone tissue destruction, compared
279 with control wild-type cells (Figures 7h,i and Figure S7). In contrast, assessment of the effect of intracardiac
280 injection of permanently NALCN-overexpressing PC-3 cells (fourth *in vivo* model) revealed that if in control
281 group (PC-3 Luc) only 18% of mice (2/11) developed one unique osteolytic lesion (both were located in the
282 fibula) then with the cells stably overexpressing NALCN (+hNALCN) as high as 64% of mice (7/11) developed
283 multiple osteolytic lesions of larger volumes (Figures S7c,d) in different bone locations (fibula, tibia, hip, humeral,
284 skull and jaw bones).
285 Overall, the results from all four *in vivo* mice models were consistent, indicating that the level of NALCN
286 expression directly correlated with the metastatic impact of PC-3 derived tumor xenografts.

287 **Discussion**

288 Present study was undertaken to assess pro-invasive potential of neuronal-type Na^+ leak channel,
289 NALCN, in prostate carcinogenesis using complex multidisciplinary approach involving: (i) prostate cancer-
290 derived cell lines for elucidating mechanistic aspects of NALCN involvement in cellular signaling promoting
291 invasive behaviors, (ii) *in vitro* animal models for determining metastatic impact of NALCN on tumor xenografts

292 and (iii) primary human prostate cancer biopsy tissues for correlating NALCN expression with clinical tumor
293 scoring and staging. In this study we report on four major findings of the utmost importance for understanding
294 the genesis of the prostate cancer invasiveness: 1) NALCN is overexpressed in highly metastatic prostate
295 cancer cell lines and primary human prostate cancer metastasis; 2) NALCN-mediated Na^+ entry in strongly
296 metastatic prostate cancer cell lines governs intracellular Ca^{2+} oscillations and promotes invadopodia formation
297 and secretion of ECM-degrading proteolytic enzymes; 3) activation of Na^+ entry via NALCN engages signaling
298 pathway involving increased mitochondrial Ca^{2+} extrusion via NCLX, decreased mitochondrial ROS production,
299 relief of SOCE inactivation by ROS, augmentation of plasma membrane SOCE and enhancement of Src kinase
300 activity; 4) in the *in vivo* mice models NALCN expression determines metastatic potential of xenograft tumors
301 and formation of bone metastasis.

302 NALCN channel was first discovered in neurons where its activity provides for constitutive influx of Na^+
303 which depolarizes V_r by about 10 mV compared to K^+ equilibrium potential (Lu *et al*, 2007). Subsequently,
304 *NALCN* gene expression was also detected in several types of human cancers (reviewed in (Cochet-Bissuel *et*
305 *al*, 2014)). However, its functional significance in carcinogenesis remained unknown. Expression of neuronal-
306 type channel, NALCN, in non-excitable cancer cells, in general, is of no surprise in view of the fact that cancer
307 cells' channelosome is known to undergo essential modification characterized by acquisition of ion channel
308 types inherent to excitability (Prevarskaya *et al*, 2018b). Thus, it is much more important to establish what cancer
309 hallmark(s) newly expressed channel(s) would promote and what intracellular signaling would be engaged.

310 Among the ion channels of cancer cells inherent to excitability, the voltage-gated, Na^+-conducting ones
311 of Na_v1 family, are specifically linked to cancer cells invasion and metastasis (House *et al*, 2010a; Roger *et al*,
312 2007). It is believed that small steady-state "window current" through these channels is the major contributor to
313 the cancer cells' depolarized V_r and increased $[Na^+]_c$ (Campbell *et al*, 2013; Gillet *et al*, 2009b; Roger *et al*,
314 2003) with both being the factors suggested to play a role in the mechanism of pro-invasive Na_v1 channels
315 action. For instance, depolarization of the V_r due to $Na_v1.5$ activity in colon cancer cells was implicated in the
316 transcriptional induction of invasion-related genes through protein kinase A (PKA), Rap1B, MEK, ERK1/2
317 signaling pathway (House *et al*, 2015, 2010b), whereas in breast cells the same was linked to modulation of F-
318 actin polymerisation and invadopodia formation (Brisson *et al*, 2013b). Furthermore, in breast cancer cells,
319 $Na_v1.5$-mediated Na^+ entry was shown to underlie intra- and extracellular pH changes via Na^+/H^+ exchanger
320 type 1 (NHE1) which in turn favored higher activity of secreted ECM-digesting proteases, cathepsins, facilitating
321 breast cancer cells invasiveness (Brisson *et al*, 2013b).

322 Taking the above into account, with the discovery of NALCN in cancer cells, an essential part of
323 depolarized V_r and enhanced Na^+ influx in these cells could be ascribed by one to the function of this channel.
324 However, our results show that in highly metastatic prostate cancer cells, coupling NALCN-mediated Na^+ entry
325 to the intracellular oscillatory-type Ca^{2+} signaling is responsible for the promotion of invasive behavior via
326 invadopodia formation and secretion of ECM-degrading proteolytic enzymes.

327 A number of Na^+-permeable channels were suggested to influence $[Ca^{2+}]_c$ events in different cell models
328 (Verkhratsky *et al*, 2018). In cancer cells, functional coupling of Na_v channels activity to intracellular Ca^{2+}
329 signaling was predicted in human colon cancer (House *et al*, 2010a). Later, it was shown that spontaneous
330 $[Ca^{2+}]_c$ oscillations in strongly metastatic human prostate and breast cancer cells were inhibited by Na_v channel
331 blockers (Rizaner *et al*, 2016). However, the molecular mechanisms coupling Na^+ influx to $[Ca^{2+}]_c$ oscillations
332 as well as their role in metastatic cell behavior remain largely unknown. The importance of Ca^{2+} signaling in
333 invasion and invadosome function is currently emerging. Yet, the identification of the specific roles of ion
334 channels at different steps of complex adhesive and degradative functions of invadosomes remains challenging.
335 For example, it has been recently shown that TRPV4 calcium channel colocalizes with β1-integrins at the
336 invadosome periphery and regulates the coupling of acto-adhesive and degradative functions(Vellino *et al*,
337 2021).

338 In prostate cancer cells we have unraveled a novel, previously not anticipated pathway composed of
339 several feedback elements through which NALCN-mediated Na^+ influx governs the oscillatory pattern of
340 intracellular Ca^{2+} signaling, which then translates into invasive behavior (Figure S8). Importantly, we have found
341 that this pathway involves mitochondrial Ca^{2+} handling, NCLX and ROS production which were recently referred
342 as the important determinants of cancer growth and metastasis (Verkhratsky *et al*, 2018; Sun *et al*, 2014). This
343 pathway (Figure S8), that could be initiated by the EGF-mediated stimulation of RTK/GPCR, involves initial Ca^{2+}
344 store depletion via derivation of Ca^{2+}-mobilizing second messenger, IP_3, with ensuing activation of
345 transmembrane SOCE. The resulting elevation of $[Ca^{2+}]_c$ facilitates NALCN translocation to PM channelosome
346 to enable NALCN-mediated Na^+ entry and increase of $[Na^+]_c$ which then promotes additional Ca^{2+} influx via RM-
347 NCX. Significant rise of $[Ca^{2+}]_c$ triggers Ca^{2+} uptake back into the ER via SERCA pump and MCU-mediated
348 Ca^{2+} uptake into mitochondria. The latter facilitates production of ROS, which is known to inhibit SERCA (Patel
349 & Brackenbury, 2015), RM-NCX (Liu & O'Rourke, 2013) and SOCE elements (Bogeski *et al*, 2012), and whose
350 action is opposed by NCLX exchanging NALCN-delivered Na^+ to mitochondrial Ca^{2+}. This positive and/or
351 negative feedback underlies generation of $[Ca^{2+}]_c$ oscillations maintaining the activity of Src, which is an

352 essential component of NALCN channelosome. Active Src, in turn, phosphorylates downstream proteins
353 (cortactin, dynamin and Tks5) recruiting them to actin polymerization regions and giving rise to invadopodia.
354 RTK/GPCR activation is also linked to activation of the Rho family GTPase, Cdc42, leading to its binding with
355 N-WASP and subsequent actin nucleation (Beaty & Condeelis, 2014). In addition, invadopodia maturation is
356 facilitated by Ca^{2+}-dependent secretion of ECM-degrading MMPs.

357 The validity of this NALCN-dependent pathway was confirmed in the *in vivo* experimentation on mice
358 xenograft tumors wherein xenografts produced by NALCN-KD cells were characterized by significant
359 downsizing of skeletal metastases, reduction in bone tissue destruction and diminution of metastasis to other
360 organs.

361 **Conclusion**

362 In this study, we identified for the first time that the expression of NALCN in highly invasive metastatic human
363 prostate carcinoma. We have found that NALCN is functional and importantly promotes invasiveness and
364 metastatic potential of prostate cancer cells by controlling the Na^{+}/Ca^{2+} signature. Specifically, we demonstrated
365 a novel NALCN-mediated mechanism of cancer cell aggressiveness whereby long-term intracellular Ca^{2+}
366 oscillations are the central players. These oscillations are controlled mainly by SOCE, NCX, NCLX, SERCA and
367 ROS, and are necessary for Src kinase activation, invadopodia formation and Ca^{2+}-dependent secretion of ECM
368 degrading enzymes. (via PIP2-WASP crosstalk). Thus, by inducing long-lasting Ca^{2+} oscillations following by
369 actine remodeling and MMP secretion, NALCN not only initiates the invasion process, but also provides
370 persistent signaling input augmenting invasiveness of aggressive cancer cells over long period of time.
371 Furthermore, our results obtained in several mice models suggest that NALCN expression promotes the
372 metastatic impact of prostate cancer *in vivo*.
373 In overall conclusion, our study identifies a novel ionic checkpoint during the metastatic transformation and
374 pinpoint NALCN as a key player governing this process in prostate cancer.

375 **Materials and methods**

376 **1. Cell culture**

377 LNCaP, DU 145 and PC-3 were from the American Type Culture Collection (ATCC®). C4-2 and PC-3M were
378 kindly provided by Dr Florence Cabon (Cancer Research Centre of Toulouse, France) and by Dr Scott Fraser
379 and Prof. Mustafa Djamgoz (Imperial College London, UK), respectively. In accordance with their origin /
380 tumorigenic potential these cancer cell lines are classified as: LNCaP – lymph node / weakly metastatic

381 (Horoszewicz *et al*, 1980); C4-2 – chimeric tumor induced by co-inoculating castrated mouse with LNCaP-
382 derived subline and bone fibroblasts / weakly metastatic (Wu *et al*, 1994); DU 145 – brain / moderately
383 metastatic (Stone *et al*, 1978); PC-3 –bone / highly metastatic (Kaighn *et al*, 1979); and PC-3M – liver
384 metastases induced by inoculating mouse with PC-3 / highly metastatic (Kozlowski *et al*, 1984). Cells were
385 cultured at 37ºC in RPMI 1640 medium (Gibco™, Thermo Fischer Scientific) supplemented with 10% fetal
386 bovine serum (Gibco™) and 2 mM L-Glutamine (Gibco™). Mouse-derived osteoblast precursor cell line MC3T3
387 E1 was cultured in MEMα medium (Gibco™) containing 10% fetal bovine serum and 1% Penicillin-Streptomycin
388 (Gibco™).

389 **2. Cell transfection**

390 Cells were transfected with 2 µg of corresponding construct or 50 nM of siRNA and 0.2 µg of pmax GFP using
391 either Nucleofector (Amaxa), or X-tremeGene HP DNA Transfection Reagent (Roche), or HiPerFect
392 Transfection Reagent (QIAGEN).

393 **3. Cloning procedures**

394 The human NALCN cDNA was previously described (Swayne *et al*, 2009) and the mCherry cDNA was obtained
395 from the pAAV-EF1a-mCherry plasmid (Addgene #114470). The human NALCN cDNA and the mCherry cDNAs
396 were subcloned in the pLV-EF1a-IRES-Blast (Addgene #85133) using standard molecular biology techniques.

397 **4. Lentiviral transduction**

398 Lentiviruses were made at the Vectorology facility of Montpellier (https://www.biocampus.cnrs.fr/index.php/en/).
399 Briefly, replication-deficient lentiviruses were produced and titrated as described by co-transfection of the
400 resulting constructs in HEK-293T cells with the HIV-1 packaging plasmid psPAX2 (Addgene #12260) and the
401 plasmid pMD2.G (Addgene #12259) that encodes the vesicular stomatitis virus glycoprotein envelope. Viruses
402 were harvested and then concentrated. Titers were calculated as described (Naldini *et al*, 1996). Once PC-3
403 cells that were seeded in 35 mm petri dishes reached the confluence of 80-90 % they were transduced with
404 120.4 µg p24 of the lentiviral suspension.

405 **5. Establishment of stable cell lines**

406 48 hours after transfection/ transduction PC-3 cells were cultured with antibiotics (700 µg/ml G418; 2 µg/ml
407 puromycin; 5 µg/ml blasticidin S). The establishment of stable cell lines was confirmed by RT-qPCR and
408 immunoblotting analysis. In order to verify the luciferase activity 150 µg/ml of D-luciferin was used.

409 **6. Chemicals**

410 Chemicals were purchased from Invitrogen Life Technologies and Sigma-Aldrich Chemicals unless stated
411 otherwise.

412 **7. RNA purification and reverse transcription polymerase chain reaction**

413 Organ tissues and cells were preserved in RNAlater™ (Sigma). Cellular RNA was purified with the NucleoSpin
414 RNA Plus Kit (Macherey-Nagel). Organ tissues were homogenized with Precellys® Tissue Homogenizer and
415 purified with TRIzol™ Reagent (Invitrogen). The cDNA from was obtained with the RNA reverse transcription
416 (Applied Biosystems) following the DNase treatment (Ambion). Conventional RT-PCR was performed by using
417 AmpliTaq Gold® (Applied Biosystems) on C1000 Touch™ Thermal Cycler (Bio-Rad), whereas quantitative (RT-
418 qPCR) - with SsoFast™ EvaGreen® (Bio-Rad) on CFX96 Touch™ Real-Time PCR Detection System.

419 **8. Immunoblotting**

420 The cells were lysed in RIPA buffer containing protease and phosphatase inhibitors, sonicated for 10 seconds
421 and centrifuged at 13000 g for 10 minutes in order to eliminate nuclei. The concentration of protein lysate was
422 measured with Pierce® BCA Protein Assay (Thermo Fisher Scientific). 1xSample Reducing Agent and 1xLDS
423 Sample Buffer (Bolt™, Thermo Fisher Scientific) were added to 50 µg of protein lysate and heated at 95^0C for
424 5 minutes. Proteins were resolved due to 3-8% Tris-acetate SDS-PAGE and transferred onto methanol-
425 activated PVDF membrane with Pierce G2 Fast Blotter (Thermo Fisher Scientific). Afterwards, the blots were
426 blocked with 5% milk TBS-T buffer (15 mM Tris-HCl, 140 mM NaCl, 0.05% Tween20®, pH 7.4) for 1 hour, and
427 then incubated with antibodies. For HRP-conjugated secondary antibodies blots were developed using
428 SuperSignal™ West Dura Extended Duration Substrate (Thermo Fisher Scientific) Images were captured with
429 Amersham Imager 600 (GE Healthcare Life Sciences).

430 **9. Cell cycle analysis**

431 Cells were fixed with ice-cold 70 % methanol for 30 minutes, resuspended in 100 µl PBS with 500 µg/ml
432 Ribonuclease A and stained with 50 µg/ml of propidium iodide for 1 hour at 4^0C. At least 10,000 events per
433 condition were processed by CyAn™ ADP Analyser FACScan flow cytometer (Becton-Dickinson).

434 **10. Cellular viability**

435 Cellular viability was evaluated with Trypan Blue Exclusion assay (Thermo Fisher Scientific).

436 **11. Apoptosis assay**

437 The level of apoptosis was estimated from the number of apoptotic nuclei revealed with Hoechst staining.

438 **12. Proliferation assay**

439 Cells were plated into 96-well plate (10^3 cells/well) and left overnight at standard growth conditions. At each
440 desired time point, cells were fixed with 50 % Trichloroacetic acid at 4^0C for 1 hour. After removing fixative
441 solution, cells were stained with 0.4 % Sulforhodamine B (Santa Cruz) in 1 % acetic acid. The dye taken up by
442 cells was then dissolved in 10 mM Tris-base, pH 10.5. The absorbance was measured at 560 nm with TriStar^2
443 Multimodal Reader LB942 (Berthold Technologies).

444 **13. Time-lapse video microscopy**

445 Cells were seeded at low density, stained with Hoechst and kept at 37°C under 5% CO_2 in an incubator chamber
446 for time-lapse video recording. Cell movements were monitored with an inverted microscope (Biostation; Nikon)
447 using a 20× objective lens. To enable tracking over long distance with high resolution, the tiling mode (4x4 or
448 8x3 tiles) of the microscope was used. The entire images were then reconstructed using FiJi Grid/Collection
449 Stitching Plugin (Schindelin *et al*, 2012).

450 **14. Cellular motility**

451 Images were acquired every 30 minutes during 48 hours. Image stacks were then analyzed using Trackmate
452 ImageJ plugin (Tinevez *et al*, 2017). For each condition, segmentation was performed on Hoechst stained
453 nucleus. The same optimized tracking parameters were used for each image series. Cells were then
454 automatically tracked using the "simple lap tracker" algorithm and, tracks coordinates and individual track mean
455 velocities were measured for each cell. Only cells tracked over a period of more than 5 hours were taken into
456 account and at least 1000 cells tracks were analysed for each condition.

457 **15. Wound-healing assay**

458 The wound-healing assay was performed in Culture-Insert IbiTreat (2 Well 35 mm high µ-Dish; Ibidi). The
459 images were acquired every 30 minutes during 48 hours. The automatic cell and wounded area detection was
460 performed using custom plug-in for ImageJ, based on previously published recommendations (Jonkman *et al.*
461 2014).

462 **16. Transwell® migration and invasion assay**

463 Cells ($75x10^3$/passage) were plated into upper compartment of 8 µm pore Transwell® inserts (Falcon™) in a
464 serum-free media, whereas lower compartment was filled with standard growth media, as a chemoattractant.

465 For invasion assay inserts were pre-coated with 1.25 mg/ml Matrigel™ Basement Membrane Matrix (Becton
466 Dickinson). After 16 hours at 37^0C, 5 % CO_2 cells were fixed in ice-cold 100% methanol and stained with 1%
467 crystal-violet in 25% methanol. Inserts were then washed and the upper area of the filter was rubbed dry to
468 eliminate the non-migrated cells. The data acquisition was made using an inverted microscope DMIRE2 (Leica)
469 at ×5 magnification. The results of the cell count from five randomly selected fields were averaged. At least two
470 inserts for each condition were analysed.

471 **17. Electrophysiological recordings**

472 Whole-cell transmembrane ion currents were recorded in perforated patch configuration at room temperature.
473 The patch pipette solution supplemented with 100 µg/ml gramicidin was composed of (in mM): 150 KCl, 1 $MgCl_2$
474 and 10 HEPES; pH adjusted to 7.3 with KOH. The cells were bathed in solution containing (in mM): 140 NaCl,
475 5 KCl, 1 MgCl2, 2 CaCl2, 5 glucose and 10 Hepes; pH adjusted to 7.3 NaOH. Patch pipettes were made from
476 borosilicate glass (WPI) and had free tip resistance 2 - 4 MΩ. The currents were recorded using an Axopatch
477 200B amplifier (Molecular Devices), and analyzed offline using pClamp (Molecular Devices) and MicroCal Origin
478 (MicroCal Software Inc., Northampton, MA, USA).

479 **18. Calcium and sodium imaging**

480 The following solutions were used (in mM): (1) the Hank's balanced salt solution (HBSS) –NaCl 150, KCl 5,
481 $MgCl_2$ 1, $CaCl_2$ 2, D-Glucose 10, HEPES 10; pH 7.4 with NaOH; (2) Na^+-free solution – choline chloride 150,
482 $MgCl_2$ 1, KCl 5, $CaCl_2$ 2, D-Glucose 5.6, HEPES 10; pH 7.4 with KOH; (3) Ca^{2+}-free solution – EGTA-NMDG 5,
483 NaCl 150, $MgCl_2$ 3, KCl 5, D-Glucose 5.6, HEPES 10; pH 7.4 with NaOH; (4) high Ca^{2+} solution – NaCl 150,
484 KCl 5, $CaCl_2$ 8, D-Glucose 5.6, HEPES 10; pH 7.4 with NaOH.

485 Cytosolic Ca^{2+} and Na^+ concentrations were measured using Fura-2-acetoxymethyl ester (AM) (Interchim) and
486 SBFI-AM (Interchim), correspondingly, as previously described (Iamshanova *et al*, 2016). Briefly, the dyes were
487 dissolved in DMSO containing 0.02% Pluronic® F127 and diluted in HBSS to the final concentrations: 1 µM and
488 7 µM, respectively. The fluorescence was excited with a xenon lamp (300 W) light using an illumination DG4
489 system (Sutter) equipped with excitation filter pair 340/26 nm and 387/11 nm (wavelength/bandwidth). The
490 fluorescence was acquired with objective 20× using Superfluor Nikon Eclipse Ti- series inverted microscope
491 equipped with the emission filter 510/84 nm and coupled to an EMCCD camera Rolera EM-C2 (Qimaging), and
492 processed using Metafluor 7.7.5.0 software (Molecular Devices).

493 **19. Confocal microscopy**

494 Confocal imaging was performed with LSM 510 META confocal workstation using a Plan-Neofluar 40× 1.3 NA
495 or Plan-Apochromat 63× 1.4 NA objectives (Carl Zeiss, Germany). The illumination intensity was attenuated to
496 0.5-6 % (depending on the laser line) with an acousto-optical tunable filter (Zeiss, Oberkochen, Germany). To
497 optimize signal quality, the pinhole was set to provide a confocal optical section 0.6–2.5 µm, depending on
498 experimental protocol. To avoid any bleed-through of the fluorescence signal in multi-staining experiments,
499 fluorochromes with well separated excitation and emission spectra were used and imaging was performed using
500 the frame-by-frame or line-by-line multitrack mode of the confocal scanner. The photomultiplier gain and offset
501 in each optical channel were set individually to achieve similar signal intensity at each channel and remove sub-
502 signal noise from the images. The adequacy of the imaging protocol applied to the multi-labeled cells was
503 confirmed by control experiments with mono-labeling.

504 Fluo-4, Mag-Fluo-4, GFP and FM1-43 were excited by 488 nm line of 500 mW Argon ion laser (Laser-Fertigung,
505 Hamburg, Germany) and the fluorescence was captured at wavelengths 505-530 nm or above 505 nm. Alexa
506 Fluor 546, mCherry, Cal-590™, DsRed2 were exited by the 543 nm line of 5 mW Helium/Neon ion laser and
507 the fluorescence was captured at wavelengths above 560 nm. CellMask™ Plsama Membrane Stain was excited
508 by 633 nm line of 15 mW Helium/Neon ion laser and the fluorescence was captured at wavelengths above 650
509 nm. The MitoSOX™ was excited by 514 nm line of a 500 mW Argon ion laser and the fluorescence was captured
510 at wavelengths above 560 nm. DAPI was excited by 405 nm blue diode laser and the fluorescence was captured
511 at 470-500 nm. Image processing was carried out using LSM 5 software (Zeiss, Oberkochen, Germany) and
512 with custom routines written in IDL (Research Systems, Inc., Boulder, CO, USA). Statistical analysis was
513 performed using MicroCal Origin (MicroCal Software Inc., Northampton, MA, USA).

514 **20. Biotinylation**

515 Protein extraction from cell surface fraction was performed with EZ-Link™ Sulfo-NHS-LC-LC-Biotin (Thermo
516 Fisher Scientific).

517 **21. Invadopodia fractionation**

518 Protein extraction from invadopodia fraction was performed as described previously (Busco *et al*, 2010).

519 **22. Src-family kinase activity assay**

520 After extraction of proteins (see above) without proteinase and phosphatase inhibitors the Src activity was
521 evaluated with ProFluor® Src-Family Kinase Assay (Promega).

522 **23. Zymography**

523 Zymography was performed using 1 % gelatin 10% SDS-PAGE. The cells were grown in FBS-free media
524 overnight. The condition media was centrifuged and the protein samples were extracted (see above) without
525 addition of reducing agents and boiling. The zymograms were developed with 0.5 % Coomassie G-250 in 30 %
526 ethanol and 10 % acetic acid.

527 **24. Tissue biopsies**

528 Normal prostate tissues (n=58) were obtained from patients without prostate cancer (PCa) underwent
529 cystoprostatectomy for bladder carcinoma.

530 Hormone naïve clinically localised cancer samples (HNCLC; n=338) were obtained from patients treated with
531 radical prostatectomy for localized PCa.

532 48 cases of castration resistant prostate cancers (CRPC) were selected from patients treated with exclusive
533 androgen deprivation therapy (ADT). Tissues were collected by transurethral resection, performed due to lower
534 urinary tract symptoms associated with local tumor progression.

535 Twenty one cases of metastatic prostate cancer were selected from patients with tissues available for analysis:
536 either lymph nodes (n=14) or bone (n=7). Among these, 5 patients (all with bone metastasis) had been
537 previously treated by hormone deprivation but revealed castration resistance.

538 Written informed consents were obtained from patients in accordance with the requirements of the medical ethic
539 committee.

540 Prostate adenocarcinoma tissue microarray (PR484) was obtained from US Biomax, Inc.

541 **25. Immuno-histochemical analysis**

542 Slides were deparaffinized, rehydrated, and heated in citrate buffer with pH 6 for antigenic retrieval. After
543 blocking for endogenous peroxidase with 3% hydrogen peroxide, the slides were incubated with the primary
544 antibodies (Table S4). Immunohistochemistry was performed using the streptavidin-biotin-peroxydase method
545 with diaminobenzidine as the chromogen (Kit LSAB, Dakocytomation, Glostrup, Denmark). Slides were finally

546 counterstained with haematoxylin. In control experiments corresponding primary antibodies were omitted from
547 the staining protocol.

548 **26. *In vivo* xenografts**

549 Orthotopic injections

550 While under isoflurane anaesthesia, 6 weeks old male NMRI Nude Mice (Charles River Laboratories) were
551 injected into the prostate gland with two PC-3 Luc cell lines (shCTL 10 mice, shNALCN 10 mice) suspended in
552 50 µl PBS. Photons emitted by cancer cells were counted by bioluminescent imaging (FimagerTM; BIOSPACE
553 Lab) and expressed in counts per minute (c.p.m.). Tumor growth was monitored by bioluminescence imaging.
554 Animal weight was measured every week. At necropsy, *ex vivo* BLI measurement for each collected organ was
555 performed within 10 min of D-luciferin intraperitoneal injection (150 mg/kg). Mice were euthanized 12 weeks
556 following implantation of tumor cells and metastatic bioluminescence was measured.

557 Intra-tibial injections

558 SCID male mice, 6 weeks of age, were housed in barrier conditions under isolated laminar flow hoods. Mice
559 bearing tumor xenografts were closely monitored for established signs of distress and discomfort. Intra-osseous
560 tumor xenograft experiments were performed as previously described (Fradet *et al*, 2013): two PC-3 Luc cell
561 lines (shCTRL 10 mice, shNALCN 10 mice) were suspended as 6 x 10^5 in 15µL PBS and injected in the bone
562 marrow cavity. Mice were sacrificed after 31 days. Radiographs (LifeRay HM Plus, Ferrania) of animals were
563 taken at that time after inoculation using X-ray (MX-20; Faxitron X-ray Corporation). Hind limbs were collected
564 for histology and histomorphometrics analysis. The bone lesion surface, that includes lytic and osteoblastic
565 regions, was measured using the computerized image analysis system MorphoExpert (Exploranova). The
566 extent of bone lesions for each animal was expressed in mm^2. Tibiae were scanned using microcomputed
567 tomography (Skyscan1174, Skyscan) with an 8.1 µM voxel size and an X-ray tube (50 kV; 80 µA) with 0.5 µm
568 aluminum filter. Three-dimensional reconstructions and rendering were performed using the manufacturer's
569 suite (Respectively, NRecon&CTVox, and Skyscan). Bone Volume/Tissue Volume (%BV/TV) includes residual
570 trabecular and remaining cortical bone.

571 Intracardiac injections

572 5-6 weeks old male NMRI Nude Mice (Charles River Laboratories) were injected into the heart with PC-3 Luc
573 (11 mice) and cells stably overexpressing NALCN (11 mice) suspended in 100 µl PBS. Computed tomography
574 scans were performed on a fast microtomograph Bruker 1278 using an image pixel size of 51.4 µm. The source

575 voltage was 59 kV (753 µA) with a 1 mm aluminium filter. A whole body acquisition consisted in two 360° scans
576 with one projection acquired each 0.5 degrees. Reconstructions were achieved with NRecon software (1.7.1.6,
577 Bruker, Germany) and images were analysed with CTvox software (3.3.0 r1403, Bruker, Germany) and
578 DataViewer software (1.5.6.2, Bruker, Germany) to vizualize respectively, the 3D skeleton volume and the
579 transversal slices of scan areas. During the exam, mice were anesthetized with a mixture consisting of
580 air/isoflurane 2% (Iso-Vet, Piramal Healthcare).

581 PTEN null mice models

582 PTEN null mice models used in this study were previously described (Parisotto *et al*, 2018). In brief, gene
583 ablation was induced by intraperitoneal injections of Tamoxifen (1 mg/mouse) daily for 5 days to 8 weeks-old
584 mice in order to generate mutant $PTEN^{(i)pe-/-}$ and $PTEN/p53^{(i)pe-/-}$ mice (pe – prostate epithelium, (i) – induced).
585 After Tamoxifen treatment 8 weeks-old mice developed prostatic intraepithelial neoplasia (PIN) in both groups,
586 whereas 72 weeks-old $PTEN^{(i)pe-/-}$ mice developed non-invasive adenocarcinoma and 18 weeks-old
587 $PTEN/p53^{(i)pe-/-}$ mice developed invasive adenocarcinoma. Respective control mice ($PTEN^{pe+/+}$ and
588 $PTEN/p53^{pe+/+}$) were subjected to corresponding Tamoxifen administration and sacrificed at the given age.

589 **27. Statistics**

590 *In vitro* data were analyzed using two-tailed Student's *t*-test to assess the differences between groups. Pairwise
591 comparisons were tested using a non-parametric two-tailed Mann-Whitney *U* test.

592 Immunohistochemical comparison between tissue biopsies groups was performed using the $\chi 2$ test for
593 categorical data and non-parametric Mann-Whitney *U* test and Kruskal-Wallis tests for continuous data.

594 *In vivo* data for mice studies were compared using non-parametric two-tailed Mann-Whitney *U* test.

595 In all cases, P values <0.05 were considered significant. Statistical analysis was performed using GraphPad
596 Prism 7 (GraphPad Software Inc., San Diego, USA), StatView, version 5.0, (Abacus Concepts, Berkeley, CA)
597 and OriginPro 2015 Beta3 software (1991–2014 OriginLab Corporation). The figures were created using
598 CorelDRAW 11.633 software (2002 Corel Corporation).

599 **28. Study approval**

600 Mice for orthotopic injections of prostate cancer cells were bred and housed at the In Vivo platform of the
601 Canceropôle Grand Ouest at Animalerie UTE- IRS1 (Nantes, France) under the animal care license no. C44278.
602 The project was approved by the French national ethical committee (APAFIS #2837-2015112314119496v2).
603 *PTEN* null mice were approved by the Institutional Animal Care and Use Committee of the Emory University
604 (Atlanta, GA), which is accredited by the American Association for the Accreditation of Laboratory Animal Care.
605 Mice for intra-tibial and intracardiac injections were purchased from Charles River and handled according to the
606 French Ministerial Decree No.87-848 of 19 October 1987.
607 Experimental protocols were approved by the Institutional Animal Care and Use Committee at the Université
608 Lyon-1 (France) (CEEA-55 Comité d'Ethique en Expérimentation Animale DR2014- 32) and at CNRS Orléans
609 (CECCOn°3) and received the number 19911 for authorization from the Ministerial Services.

610 **Acknowledgments**

611 We thank F. Cabon (Cancer Research Centre of Toulouse, France) and S. Fraser (Imperial College London,
612 United Kingdom) for C4-2 and PC-3M cell lines, accordingly. We thank E. Dewailly (Inserm U1003, University
613 of Lille, France) for help with reagents and cellular biology methods. We thank C. Slomianny, E. Richard and
614 A.-S. Lacoste of the BICeL- Campus Scientific City Facility for access to instruments and technical advices. We
615 are indebted to the Research Federation FRABio (University of Lille, CNRS, FR 3688, FRABio, Biochimie
616 Structurale et Fonctionnelle des Assemblages Biomoléculaires) for providing the scientific and technical
617 environment conducive to achieving this work. We thank Dr. C. Lemmers (Vectorology facility, PVM, Biocampus
618 Montpellier, CNRS UMS3426) for lenvirus production. We thank C. Lagadec and R.-A. Toillon for help with their
619 flow-cytometry facility (Inserm U908, University of Lille, France). We thank Daniel Metzger (Inserm U1258,
620 University of Strasbourg, France) and Emmanuelle Germain (Inserm U1003, University of Lille, France) for
621 providing us with cDNA from *PTEN* null mice model. We also thank Pr. Stephan Reshkin (University of Bari)
622 and Pr. Philippe Chavrier (Curie Institute, Paris) for helpful discussions.

623 **Author contributions**

624 O.I., D.G., Ar.M. and N.P. conceived and planned the study. O.I. and A.F. designed, performed and analyzed
625 cell culture assays (e.g. cell cycle analysis, cellular viability, apoptosis, proliferation, cellular motility, wound-
626 healing, Transwell® migration and invasion assays) as well as invadopodia fractionation and Src-family kinase
627 activity assay. D.G. designed, performed and analyzed confocal microscopy experiments. O.I., A.F., R.D., E.D.
628 and A.B. designed, performed and analyzed cellular and molecular biology experiments (e.g. RT-qPCR,
629 immunoblotting, biotinylation, zymography). G.S., P.M. and A.F. designed, performed and analyzed

electrophysiological recordings. O.I., A.F. and P.M. designed, performed and analyzed Ca^{2+} and Na^{+} imaging experiments. Ar.M. constructed NALCN-expressing plasmids. V.L. participated in choosing the epitope for antibody against NALCN. A.H. participated in the screening of shNALCN clones. L.A. and A.B. amplified and extracted plasmid constructs. H.I. and Ar.M. established PC-3 cell line stably overexpressing NALCN. C.S. designed, performed and analyzed time-lapse video microscopy, cellular motility and wound-healing experiments. L.B. and Se.R. designed, performed and analyzed measurements of intracellular pH. T.O. and S.M.-L. designed, performed and analyzed tumor growth and metastases in mice after orthotopical injections of PC-3 cells. Se.R., S.C., St.R., M.L., J.S. and S.L. designed, performed and analysed the bone metastatic model in mice after intracardiac injections of PC-3 cells. S.G. and P.C. designed, performed and analyzed osteoblasts-mediated invasion of PC-3 cells, intratibial injections of the latter and analysis of produced bone lesions. Ad.M. and P.G. performed immunohistochemical staining of prostate adenocarcinoma tissue microarray and V.L. helped them. G.F.-H. performed immunohistochemical staining of prostate biopsies from patients and analyzed the correlation between expression of different proteins. O.I., D.G., and N.P. wrote the manuscript and O.I., D.G., A.F., M.D., Se.R., Ar.M., P.C. and G.F.-H. reviewed it.

Competing interest

We declare that the authors don't have any competing interests related to this manuscript. All authors have approved the manuscript for submission to EMBO Jounal.

Funding

O. I. was funded by the Ligue Nationale Contre le Cancer, France (GB/MA/CD 11813) and Laboratory of Excellence in Ion Channel Science and Therapeutics. H. I. is co-funded by both Naresuan University (Thailand) and the French Embassy in Thailand. The research in the authors' laboratory is supported by INSERM, la Ligue Nationale Contre le Cancer (équipe labellisée), Institute for Cancer Research (grant 2014-166); Le Ministere de l'Education Nationale, the Region Nord/Pas-de-Calais, la Fondation de Recherche Medicale, and l'Association pour la Recherche sur le Cancer.

The paper explained

Our study is focused on molecular identification of Na+/Ca2+ signaling pathway driving metastatic behavior of prostate cancer cells. Indeed, metastasis is the main cause of prostate cancer patient's mortality. It is, therefore, vital to understand the processes underlying the progression of prostate cancer to aggressive metastatic phenotypes. Alteration of ionic homeostasis driven by aberrant ion channel expression/function, referred to as 'oncochannelopathies' (Prevarskaya et al., Physiological Reviews 2018), is one of the important features of the

660 development of invasive tumor phenotype. However, the causal link between aberrant ionic homeostasis and
661 invasion of cancer cells (in particular in prostate cancer) as well as the underlying molecular mechanisms remain
662 poorly understood.
663 Using variety of in vitro and in vivo approaches, we demonstrate that strongly metastatic cancer cells acquire
664 specific ionic signature that facilitates persistent invasion. In particular, we show how Na+ influx via the leak
665 channel, NALCN, initially identified in neurons, gives rise to long-lasting Ca2+ oscillations (in cytoplasm,
666 endoplasmic reticulum and mitochondria), ROS production and promotes invasion.
667 We also show that modulation of NALCN bioavailability strongly affects prostate cancer progression in vivo. As
668 our study provides an example of application and combination of innovative experimental approaches at multiple
669 levels of assessment allowing uncovering the fundamental mechanisms of carcinogenesis.
670 **Availability for supporting data**
671 We declare that the material of the present manuscript has been neither published nor submitted for publication
672 elsewhere, in part or in whole. All data generated or analysed during this study are included in this published
673 article (and its supplementary information files).
674 **References**
675 Beaty BT & Condeelis J (2014) Digging a little deeper: The stages of invadopodium formation and maturation.
676 *Eur J Cell Biol* 93: 438–444
677 Ben-Kasus Nissim T, Zhang X, Elazar A, Roy S, Stolwijk JA, Zhou Y, Motiani RK, Gueguinou M, Hempel N,
678 Hershfinkel M, *et al* (2017) Mitochondria control store-operated Ca 2+ entry through Na + and redox
679 signals. *EMBO J* 36: 797–815
680 Biankin A V, Waddell N, Kassahn KS, Gingras M, Muthuswamy LB, Johns AL, Miller DK, Wilson PJ, Wu J,
681 Chang DK, *et al* (2012) Pancreatic cancer genomes reveal aberrations in axon guidance pathway genes.
682 *Nature* 491: 399–405
683 Bogeski I, Kilch T & Niemeyer BA (2012) ROS and SOCE: Recent advances and controversies in the
684 regulation of STIM and Orai. *J Physiol* 590: 4193–4200
685 Brisson L, Driffort V, Benoist L, Poet M, Counillon L, Antelmi E, Rubino R, Besson P, Labbal F, Chevalier S, *et*
686 *al* (2013a) NaV1.5 Na+ channels allosterically regulate the NHE-1 exchanger and promote the activity of
687 breast cancer cell invadopodia. *J Cell Sci* 126: 4835–4842
688 Brisson L, Driffort V, Benoist L, Poet M, Counillon L, Antelmi E, Rubino R, Besson P, Labbal F, Chevalier S, *et*
689 *al* (2013b) NaV1.5 Na+ channels allosterically regulate the NHE-1 exchanger and promote the activity of

690 breast cancer cell invadopodia. *J Cell Sci* 126: 4835–4842
691 Busco G, Cardone RA, Greco MR, Bellizzi A, Colella M, Antelmi E, Mancini MT, Dell'Aquila ME, Casavola V,
692 Paradiso A, *et al* (2010) NHE1 promotes invadopodial ECM proteolysis through acidification of the peri-
693 invadopodial space. *FASEB J* 24: 3903–3915
694 Campbell TM, Main MJ & Fitzgerald EM (2013) Functional expression of the voltage-gated Na+-channel
695 Nav1.7 is necessary for EGF-mediated invasion in human non-small cell lung cancer cells. *J Cell Sci*
696 126: 4939–4949
697 Cochet-Bissuel M, Lory P & Monteil A (2014) The sodium leak channel, NALCN, in health and disease. *Front*
698 *Cell Neurosci* 8: 1–17
699 Djamgoz MBA, Fraser SP & Brackenbury WJ (2019) In vivo evidence for voltage-gated sodium channel
700 expression in carcinomas and potentiation of metastasis. *Cancers (Basel)* 11
701 Fradet A, Sorel H, Depalle B, Serre CM, Farlay D, Turtoi A, Bellahcene A, Follet H, Castronovo V, Clézardin
702 P, *et al* (2013) A New Murine Model of Osteoblastic/Osteolytic Lesions from Human Androgen-Resistant
703 Prostate Cancer. *PLoS One* 8: e75092
704 Friedl P & Wolf K (2008) Tube travel: The role of proteases in individual and collective cancer cell invasion.
705 *Cancer Res* 68: 7247–7249
706 Gillet L, Roger S, Besson P, Lecaille F, Gore J, Bougnoux P, Lalmanach G & Le Guennec JY (2009a)
707 Voltage-gated sodium channel activity promotes cysteine cathepsin-dependent invasiveness and colony
708 growth of human cancer cells. *J Biol Chem* 284: 8680–8691
709 Gillet L, Roger S, Besson P, Lecaille F, Gore J, Bougnoux P, Lalmanach G & Le Guennec JY (2009b)
710 Voltage-gated sodium channel activity promotes cysteine cathepsin-dependent invasiveness and colony
711 growth of human cancer cells. *J Biol Chem* 284: 8680–8691
712 Haneder S, Giordano FA, Konstandin S, Brehmer S, Buesing KA, Schmiedek P, Schad LR, Wenz F,
713 Schoenberg SO & Ong MM (2015) ^{23}Na-MRI of recurrent glioblastoma multiforme after intraoperative
714 radiotherapy: technical note. *Neuroradiology* 57: 321–326
715 Horoszewicz JS, Leong SS, Chu TM, Wajsman ZL, Friedman M, Papsidero L, Kim U, Chai LS, Kakati S, Arya
716 SK, *et al* (1980) The LNCaP cell line - a new model for studies on human prostatic carcinoma. *Prog Clin*
717 *Biol Res* 37: 115–132
718 House CD, Vaske CJ, Schwartz AM, Obias V, Frank B, Luu T, Sarvazyan N, Irby R, Strausberg RL, Hales
719 TG, *et al* (2010a) Voltage-gated Na+channel SCN5A is a key regulator of a gene transcriptional network

720 that controls colon cancer invasion. *Cancer Res* 70: 6957–6967
721 House CD, Vaske CJ, Schwartz AM, Obias V, Frank B, Luu T, Sarvazyan N, Irby R, Strausberg RL, Hales
722 TG, *et al* (2010b) Voltage-Gated Na + Channel SCN5A Is a Key Regulator of a Gene Transcriptional
723 Network That Controls Colon Cancer Invasion. *Cancer Res* 70: 6957–6967
724 House CD, Wang B-D, Ceniccola K, Williams R, Simaan M, Olender J, Patel V, Baptista-Hon DT, Annunziata
725 CM, Silvio Gutkind J, *et al* (2015) Voltage-gated Na+ Channel Activity Increases Colon Cancer
726 Transcriptional Activity and Invasion Via Persistent MAPK Signaling. *Sci Rep* 5: 11541
727 Iamshanova O, Mariot P, Lehen'kyi V & Prevarskaya N (2016) Comparison of fluorescence probes for
728 intracellular sodium imaging in prostate cancer cell lines. *Eur Biophys J* 45: 765–777
729 Jonkman JEN, Cathcart JA, Xu F, Bartolini ME, Amon JE, Stevens KM & Colarusso P (2014) An introduction
730 to the wound healing assay using live-cell microscopy. *Cell Adhes Migr* 8: 440–451
731 doi:10.4161/cam.36224 [PREPRINT]
732 Kaighn ME, Narayan KS, Ohnuki Y, Lechner JF & Jones LW (1979) Establishment and characterization of a
733 human prostatic carcinoma cell line (PC-3). *Invest Urol* 17: 16–23
734 Kozlowski JM, Fidler IJ, Campbell D, Xu ZL, Kaighn ME & Hart IR (1984) Metastatic behavior of human tumor
735 cell lines grown in the nude mouse. *Cancer Res* 44: 3522–3529
736 Liu T & O'Rourke B (2013) Regulation of the Na+/Ca2+ exchanger by pyridine nucleotide redox potential in
737 ventricular myocytes. *J Biol Chem* 288: 31984–31992
738 Lu B, Su Y, Das S, Liu J, Xia J & Ren D (2007) The Neuronal Channel NALCN Contributes Resting Sodium
739 Permeability and Is Required for Normal Respiratory Rhythm. *Cell* 129: 371–383
740 Lu B, Su Y, Das S, Wang H, Wang Y, Liu J & Ren D (2009) Peptide neurotransmitters activate a cation
741 channel complex of NALCN and UNC-80. *Nat Rev Cancer* 457: 741–744
742 Lu B, Zhang Q, Wang H, Wang Y, Nakayama M & Ren D (2010) Extracellular Calcium Controls Background
743 Current and Neuronal Excitability via an UNC79-UNC80-NALCN Cation Channel Complex. *Neuron* 68:
744 488–499
745 Monteith GR, Prevarskaya N & Roberts-Thomson SJ (2017) The calcium-cancer signalling nexus. *Nat Rev*
746 *Cancer* 17: 367–380
747 Naldini L, Blomer U, Gage FH, Trono D & Verma IM (1996) Efficient transfer, integration, and sustained long-
748 term expression of the transgene in adult rat brains injected with a lentiviral vector. *Proc Natl Acad Sci U*
749 *S A* 93: 11382–11388

750 Parisotto M, Grelet E, Bizri R El, Dai Y, Terzic J, Eckert D, Gargowitsch L, Bornert JM & Metzger D (2018)
751 PTEN deletion in luminal cells of mature prostate induces replication stress and senescence in vivo. *J*
752 *Exp Med* 215: 1749–1763
753 Patel F & Brackenbury WJ (2015) Dual roles of voltage-gated sodium channels in development and cancer.
754 *Int J Dev Biol* 59: 357–366
755 Prevarskaya N, Skryma R & Shuba Y (2011) Calcium in tumour metastasis: New roles for known actors. *Nat*
756 *Rev Cancer* 11: 609–618
757 Prevarskaya N, Skryma R & Shuba Y (2018a) Ion channels in cancer: Are cancer hallmarks
758 oncochannelopathies? *Physiol Rev* 98: 559–621
759 Prevarskaya N, Skryma R & Shuba Y (2018b) Ion Channels in Cancer: Are Cancer Hallmarks
760 Oncochannelopathies? *Physiol Rev* 98: 559–621
761 Qin F, Siwik DA, Pimentel DR, Morgan RJ, Biolo A, Tu VH, James Kang Y, Cohen RA & Colucci WS (2014)
762 Cytosolic H2O2 mediates hypertrophy, apoptosis, and decreased SERCA activity in mice with chronic
763 hemodynamic overload. *Am J Physiol - Hear Circ Physiol* 306: 1453–1463
764 Rizaner N, Onkal R, Fraser SP, Pristerá A, Okuse K & Djamgoz MBA (2016) Intracellular calcium oscillations
765 in strongly metastatic human breast and prostate cancer cells: control by voltage-gated sodium channel
766 activity. *Eur Biophys J* 45: 735–748
767 Roger S, Besson P & Le Guennec J-Y (2003) Involvement of a novel fast inward sodium current in the
768 invasion capacity of a breast cancer cell line. *Biochim Biophys Acta* 1616: 107–111
769 Roger S, Rollin J, Barascu A, Besson P, Raynal P-I, Iochmann S, Lei M, Bougnoux P, Gruel Y & Le Guennec
770 J-Y (2007) Voltage-gated sodium channels potentiate the invasive capacities of human non-small-cell
771 lung cancer cell lines. *Int J Biochem Cell Biol* 39: 774–786
772 Schindelin J, Arganda-Carreras I, Frise E, Kaynig V, Longair M, Pietzsch T, Preibisch S, Rueden C, Saalfeld
773 S, Schmid B, *et al* (2012) Fiji: An open-source platform for biological-image analysis. *Nat Methods* 9:
774 676–682 doi:10.1038/nmeth.2019 [PREPRINT]
775 Shah K, Patel S, Mirza S & Rawal RM (2018) Unravelling the link between embryogenesis and cancer
776 metastasis. *Gene* 642: 447–452
777 Stone KR, Mickey DD, Wunderli H, Mickey GH & Paulson DF (1978) Isolation of a human prostate carcinoma
778 cell line (DU 145). *Int J Cancer* 21: 274–281
779 Sun J, Lu F, He H, Shen J, Messina J, Mathew R, Wang D, Sarnaik AA, Chang W, Kim M, *et al* (2014)

780 STIM1- and Orai1-mediated Ca2+ oscillation orchestrates invadopodium formation and melanoma
781 invasion. *J Cell Biol* 207: 535–548
782 Swayne LA, Mezghrani A, Varrault A, Chemin J, Bertrand G, Dalle S, Bourinet E, Lory P, Miller RJ, Nargeot J,
783 *et al* (2009) The NALCN ion channel is activated by M3 muscarinic receptors in a pancreatic β-cell line.
784 *EMBO Rep* 10: 873–880
785 Tinevez JY, Perry N, Schindelin J, Hoopes GM, Reynolds GD, Laplantine E, Bednarek SY, Shorte SL &
786 Eliceiri KW (2017) TrackMate: An open and extensible platform for single-particle tracking. *Methods* 115:
787 80–90
788 Vellino S, Oddou C, Rivier P, Boyault C, Hiriart-Bryant E, Kraut A, Martin R, Coute Y, Knölker HJ, Valverde
789 MA, *et al* (2021) Cross-talk between the calcium channel TRPV4 and reactive oxygen species interlocks
790 adhesive and degradative functions of invadosomes. *J Cell Biol* 220
791 Verkhratsky A, Khananshvili D, Trebak M, Sekler I & Perocchi F (2018) Crosslink between calcium and
792 sodium signalling. *Exp Physiol* 103: 157–169
793 Wu H, Hsieh J, Gleave M, Brown N, Pathak S & Chung W (1994) Derivation of androgen-independent human
794 LNCaP prostatic cancer cell sublines: Role of bone stromal cells. *Int J Cancer* 57: 406–412
795 Zaric O, Pinker K, Zbyn S, Strasser B, Robinson S, Minarikova L, Gruber S, Farr A, Singer C, Helbich TH, *et*
796 *al* (2016) Quantitative Sodium MR Imaging at 7 T: Initial Results and Comparison with Diffusion-
797 weighted Imaging in Patients with Breast Tumors. *Radiology* 280: 39–48

798 **Main figures and legends**

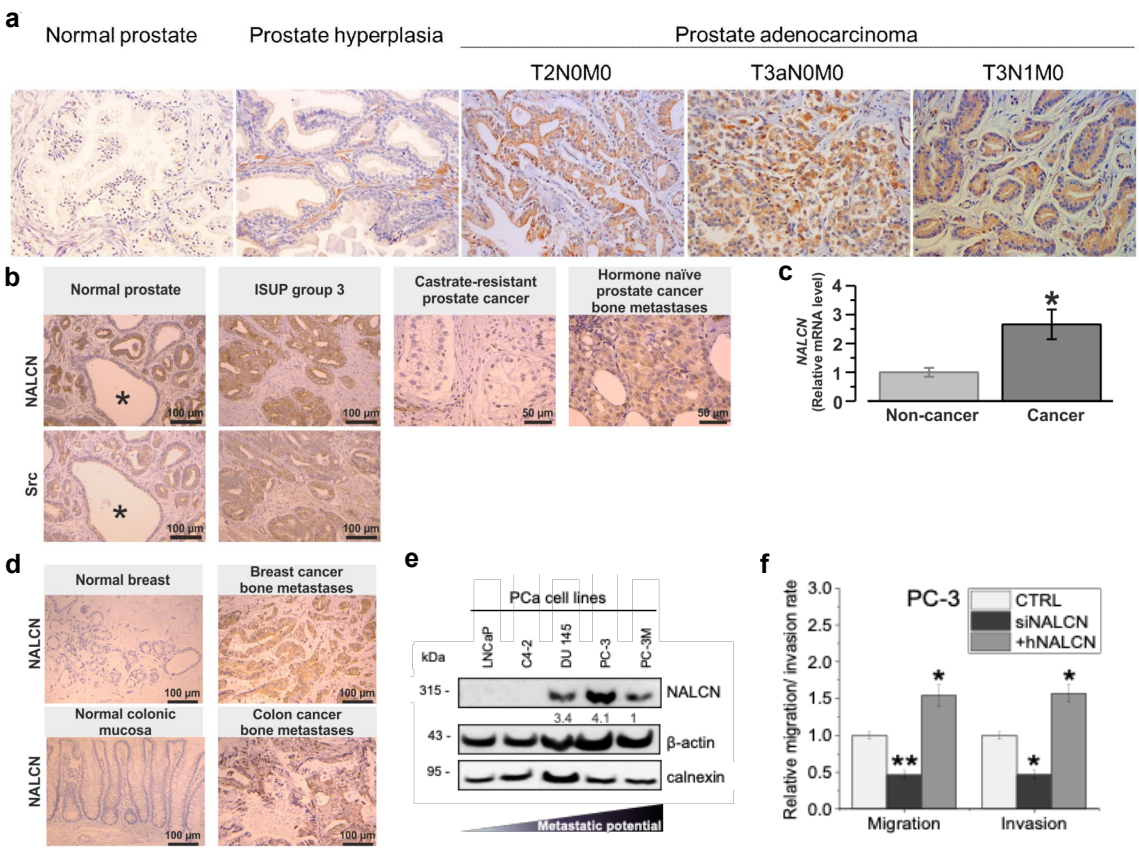

Figure 1: NALCN promotes prostate cancer progression

(a) Immunohistochemical positive staining for NALCN in human prostate adenocarcinoma tissues, but not in normal or hyperplastic prostate tissues (tissue microarray: PR484, US Biomax, Inc). T2N0M0 - tumor invaded submucosa without any regional or distant metastases (stage II); T3aN0M0 – tumor had broken through the capsule of the prostate gland and invaded through muscularis propria (stage III); T3N1M0 – tumor invaded through muscularis propria with 1 to 3 regional lymph node metastases (stage IV). (b) Immunohistochemistry: significant correlation (P<0.0001) between positive staining of NALCN and Src in clinically localized prostate cancer, but not in non-cancerous (*) prostate. Note smooth muscle fiber staining as positive internal control for NALCN. (c) RT-qPCR: NALCN mRNA level in cancerous vs. non-cancerous prostate biopsies (n=28). Data are mean±S.E.M. *P<0.05, two-tailed Mann-Whitney U test. (d) Immunohistochemistry: positive staining of NALCN in bone metastases produced by breast and colon cancers, but not in normal corresponding tissues. (e) NALCN protein level in human prostate cancer cell lines. Data are normalised to β-actin and calnexin and are presented as mean values±SEM of three independent experiments (n=3). (f) Transwell® migration and Matrigel invasion assays after transient NALCN suppression and overexpression. Control cells were transfected for 72 hours whether with siRNA targeting firefly luciferase (CTRL), whereas NALCN depleted

cells with siRNA (siNALCN) and NALCN overexpressing cells (+hNALCN). Data are presented as mean±S.E.M of four independent experiments. *P<0.05, two-tailed Mann-Whitney U test.

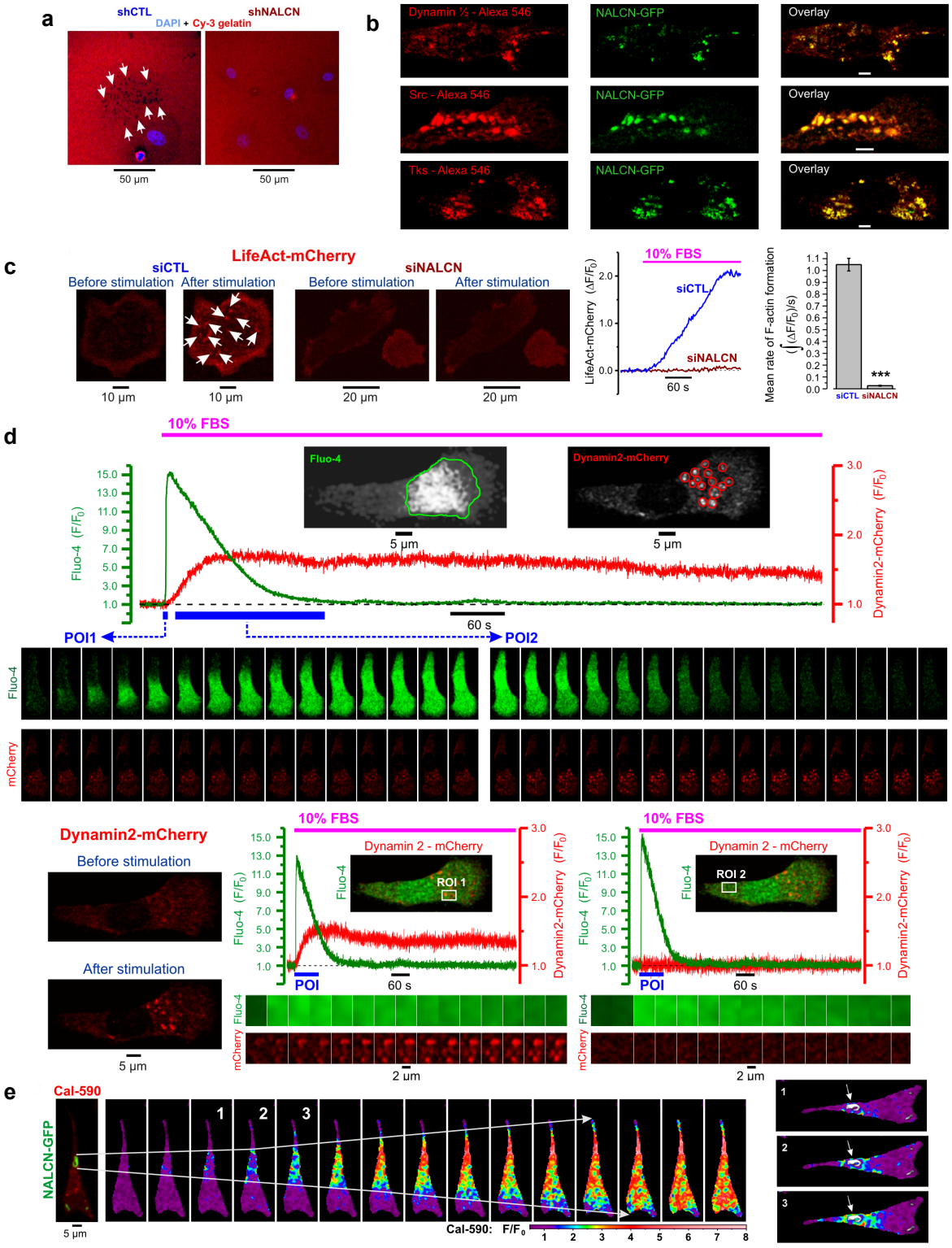

Figure 2. Spatial distribution of NALCN and its signaling input in PC-3 Cells.

(a) NALCN knockdown suppresses invadopodium formation reported by Cy3-fluorescent gelatin degradation

820 (arrows). Confocal images of Cy3 (red) and DAPI (blue; nuclei) fluorescence in control (shCTL) and shNALCN
821 48 hours after plating the cells on gelatin. (b) Co-localisation of NALCN with invadopodia markers: Dynamin
822 (top), Src (middle) and Tks (bottom). (c) NALCN silencing suppresses invadopodial precursor assembly
823 (arrows: F-actin-enriched regions reported by LifeAct-mCherry). Left: near-cell-bottom confocal images
824 captured before and 3 min after stimulation with 10% fetal bovine serum (FBS). Middle: corresponding traces
825 of relative changes in mCherry fluorescence. Right: mean rate of F-actin formation estimated as signal mass (
826) per second in cells transfected with siCTL (n=93) and with siNALCN (n=140). Data: mean±S.E.M.
827 ***P<0.001, two-tailed Student's t-test. (d) Plot (top) shows temporal profiles of self-normalised fluorescence
828 intensity (F/F0) of fluo-4 (green), averaged within outlined region (inset: left, green outline), and mCherry
829 (red), averaged within 14 circles (inset: right, red outlines). The galleries (bottom) show confocal images of
830 fluo-4 and mCherry fluorescence captured during two periods of interests, POIs (depicted by blue bars on the
831 plot): POI1 (left gallery: every image) and POI2 (right gallery: every 100th image). Bottom left: confocal
832 images of Dynamin2-mCherry fluorescence captured before and 3 min after stimulation with 10% FBS. Middle
833 and right: plots relate the dynamics of [Ca2+]c changes (Fluo-4) to formation of dynamin puncta (Dynamin2-
834 mCherry) at two regions of interests (ROIs) (insets); the galleries (below) show every 40th image (after 90°
835 rotation) during the POIs (plots: blue bars). (e) Top: the overlay of NALCN-GFP and Cal-590 images (left) is
836 related to the gallery of self-normalized rainbow-coded Cal-590 images showing [Ca2+]c response to 10%
837 FBS. Right: 3 rainbow-coded Cal-590 images are superimposed on grey-coded NALCN-GFP image. Arrows:
838 NALCN-enriched structure.

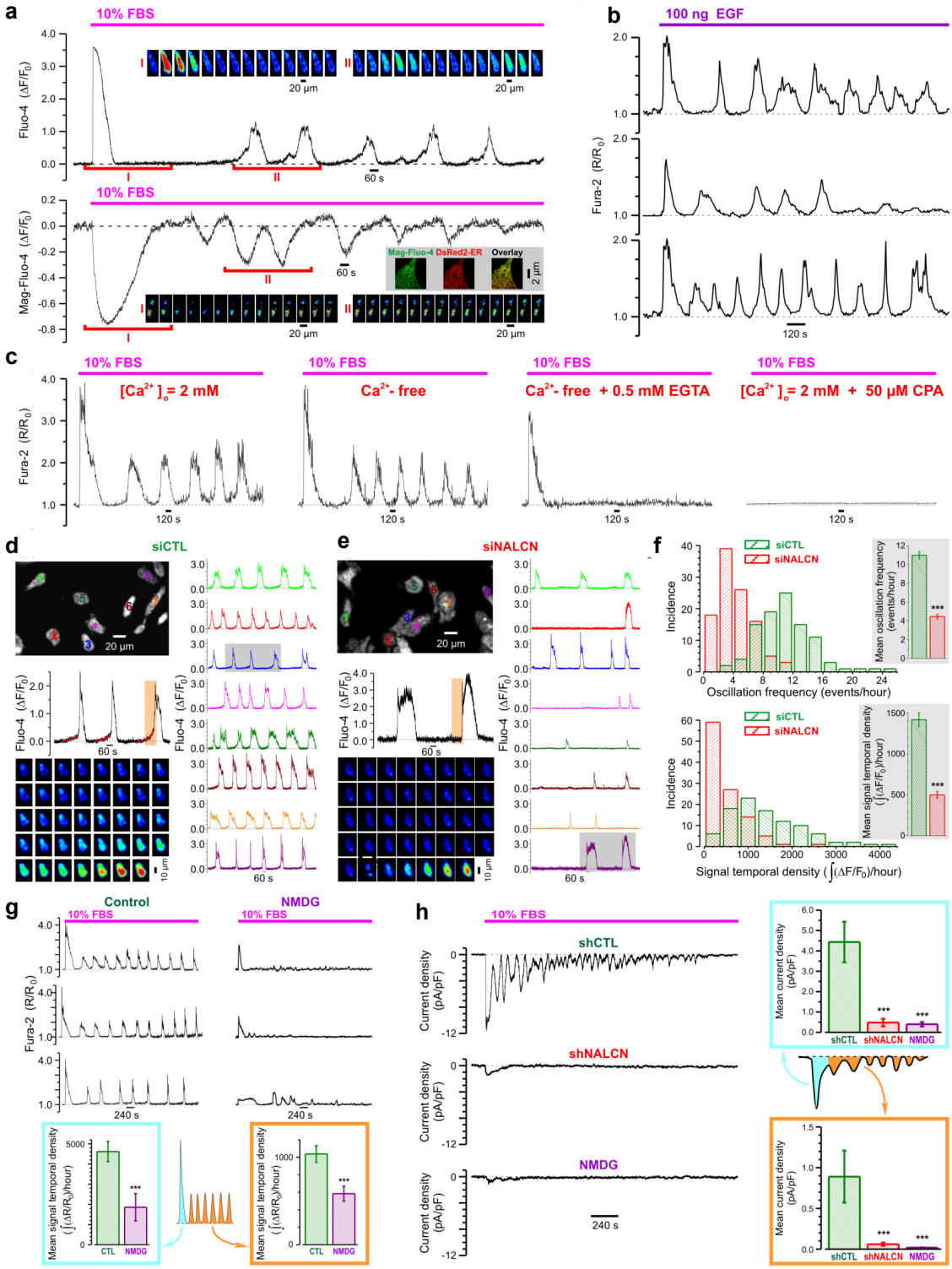

Figure 3. NALCN Regulates Ca2+ Oscillations in PC-3 Cells.

(a) FBS-induced transient cytosolic Ca2+ ([Ca2+]c) elevations (Fluo-4, top) are associated with transient decreases of Ca2+ concentration in endoplasmic reticulum ([Ca2+]ER) (Mag-Fluo-4, bottom). The galleries (insets) show every 100th image during the highlighted periods (I and II, respectively). Visualisation of the ER

844 with pDsRed2-ER vector confirms the ER origin of Mag-Fluo-4 signal (grey background inset: confocal images
845 of cell fragment). (b) Sample traces of epithelial growth factor (EGF)-induced [Ca2+]c responses (Fura-2). (c)
846 Contribution of Ca2+ influx and Ca2+ release to FBS-induced [Ca2+]c response (Fura-2) illustrated by sample
847 traces (left to right): control, nominally Ca2+-free or EGTA-supplemented solutions, and Ca2+-containing
848 solution but depleted Ca2+ stores. (d and e) [Ca2+]c oscillations reported by confocal time-series imaging of
849 Fluo-4 fluorescence in FBS-exposed PC-3 cells pre-treated with siCTL (d) or siNALCN (e) for 72 hours. The
850 trace colours (right) correspond to the colour of the cell number (top left). Highlighted (grey background)
851 periods are presented on enlarged plots (left middle) to emphasize that NALCN suppression abolishes
852 “pacemaker events” observed in control (fitted red curves). The galleries (left bottom) show every 3rd image
853 during the highlighted periods (left middle: orange background). (f) The histograms compare the oscillation
854 frequency (top) and signal temporal density (bottom) distributions for siCTL (n=98) and siNALCN (n=107).
855 Insets: corresponding mean±S.E.M. ***P<0.001, two-tailed Student’s t-test. (g) FBS-induced [Ca2+]c
856 response (Fura-2, ΔR/R0) is attenuated following reduction of extracellular Na+ concentration ([Na+]o) to 19.5
857 mM (substitution with NMDG). (h) FBS-induced inward current (perforated patch, Vh=-80 mV) is suppressed
858 following pre-treatment with shNALCN or reduction of [Na+]o to 13 mM (substitution with NMDG). The bar
859 diagram plots: mean signal temporal densities (g, n=20-23) and mean current densities (h, n=4-6) during initial
860 transient (cyan) and oscillations (orange). Data: mean±S.E.M. ***P<0.001, two-tailed Mann-Whitney U test.

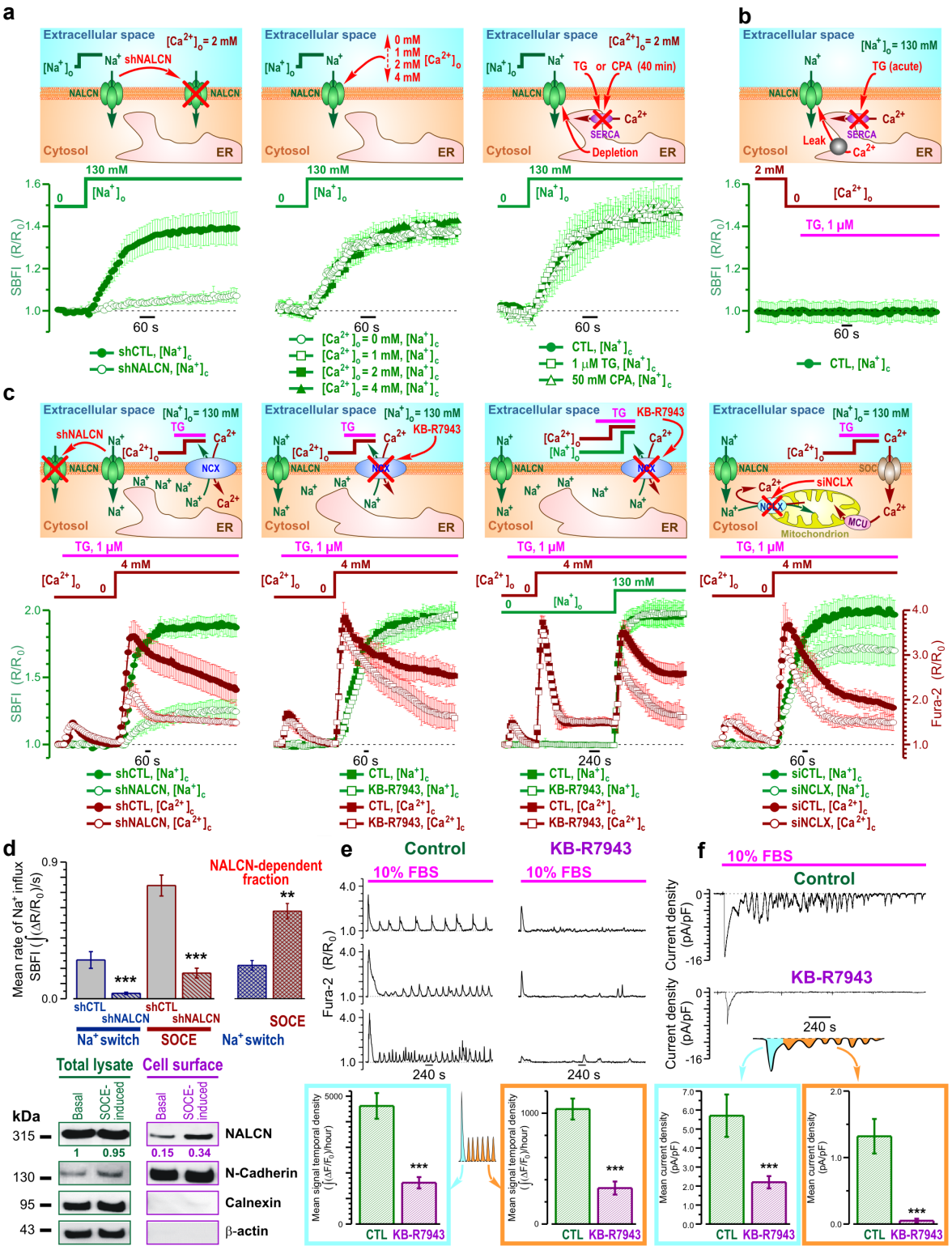

Figure 4. Interplay between SOCE, NALCN, NCX and NCLX in PC-3 Cells.

(a and b) Extracellular Na+ concentration ([Na+]o) changes reported by ratiometric Na+ indicator SBFI following (a) [Na+]o switch from 0 to 130 mM and (b) application of 1 μM thapsigargin (TG), the sarco/endoplasmic reticulum (SERCA) inhibitor uncoupling the endoplasmic reticulum (ER) Ca2+ leak from

866 Ca2+ re-uptake into the ER. In (a) the effect of (left to right): NALCN knockdown, extracellular Ca2+
867 concentration ([Ca2+]o) and Ca2+ store depletion. (c) Store-operated Ca2+ entry (SOCE)-induced changes of
868 cytosolic Na+ concentration ([Na+]c) (SBFI) and cytosolic Ca2+ concentration ([Ca2+]c) (Fura-2); the effect of
869 (left to right): NALCN knockdown, the reverse-mode plasmalemmal Na+/Ca2+ exchanger (RM-NCX) inhibitor
870 KB-R7943 (1 μM) at [Na+]o=130 mM and [Na+]o stepped from 0 to 130 mM following SOCE activation, and
871 knockdown of the mitochondrial Na+/Ca2+ exchanger (siNCLX). In (a-c) cartoons (top) highlight experimental
872 design and plots (bottom) show traces (mean±S.E.M; n=45-501) of SBFI (olive) and Fura-2 (wine)
873 fluorescence with the axes (R/R0) presented in corresponding colour. (d) SOCE addresses NALCN to plasma
874 membrane. Plots (top) compare mean rates of Na+ influx induced by [Na+]o-switch (n=283-360) and SOCE
875 (n=180-216), and their shNALCN-sensitive fractions. Immunoblotting (bottom) compares NALCN expression
876 in total cell lysates and biotinylated fractions before and following SOCE induction. Numbers show (in
877 corresponding colour) mean values (n=3) of NALCN protein levels (band intensity) normalized to N-Cadherin,
878 Calnexin and β-actin. (e and f) KB-R7943 (1 μM) attenuates: (e) [Ca2+]c responses (Fura-2, R/R0) and (f)
879 inward current (perforated patch, Vh=-80 mV) induced by 10% FBS. The bar diagram plots: mean signal
880 temporal densities (e, n=20) and mean current densities (f, n=6-8) during initial transient (cyan) and
881 oscillations (orange). Data are mean±S.E.M. **P<0.01, ***P<0.001, two-tailed Mann-Whitney U test.

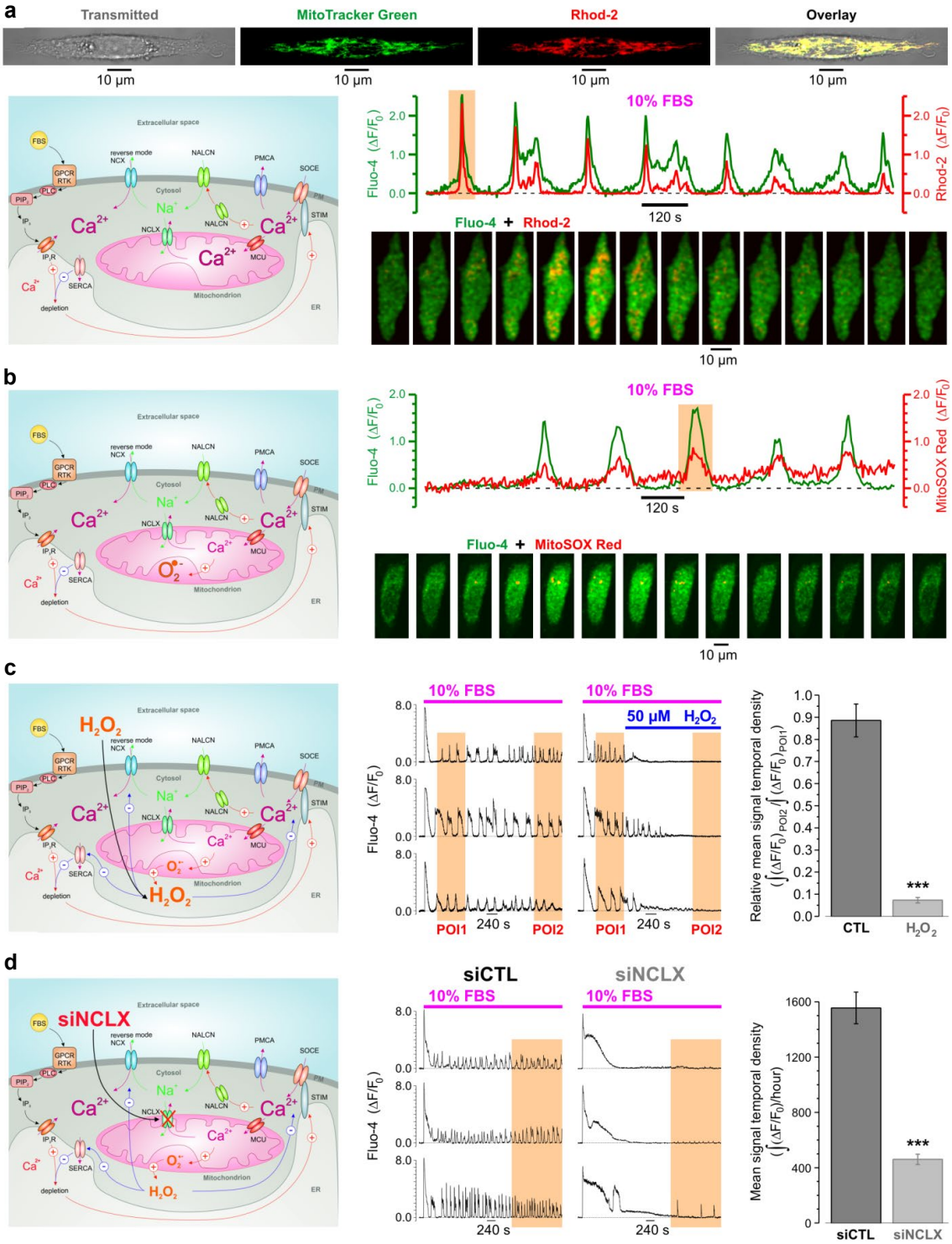

Figure 5. NALCN and Recruitment of Mitochondria to [Ca2+]c Oscillations in PC-3 Cells.

Cartoons (left) highlight experimental design and assessed signaling pathways. Note that Na+ delivered to the cytosol by NALCN, on the one hand, activates reverse mode (RM-) of NCX, while on the other hand, is exchanged by NCLX to Ca2+ thus restricting elevation of [Ca2+] in mitochondria ([Ca2+]mito) and, hence, production of superoxide (O2-) and H2O2, which is known to inhibit SERCA, RM-NCX and SOCE elements.

888 (a) Top: visualisation of mitochondria with MitoTracker Green confirms mitochondrial origin of Rhod-2 signal.
889 Middle: Fetal bovine serum (FBS)-induced [Ca2+]c oscillations (Fluo-4) are associated with [Ca2+]mito
890 oscillations (Rhod-2). Bottom: every 2nd image from the highlighted (middle) period. (b) Top: FBS-induced
891 [Ca2+]c oscillations (Fluo-4) are associated with oscillations in O2- production by mitochondria (MitoSOX
892 Red). Bottom: every 3rd image from the highlighted (middle) period. (c) O2- metabolite H2O2 suppresses
893 FBS-induced [Ca2+]c oscillations (Fluo-4). Left: representative traces. Right: mean signal (Fluo-4) temporal
894 density during POI2 was normalized to that during POI1 in control (n=58) and in 50 μM of H2O2 (n=74), and
895 compared. (d) Suppression of NCLX with siRNA (siNCLX) attenuates [Ca2+]c oscillations (Fluo-4). Left:
896 representative traces. Right: mean signal (Fluo-4) temporal densities during highlighted periods were
897 compared in control (n=18) and following 48 h pre-treatment with siNCLX (n=17). Data are mean±S.E.M.
898 ***P<0.001, two-tailed Mann-Whitney U test.

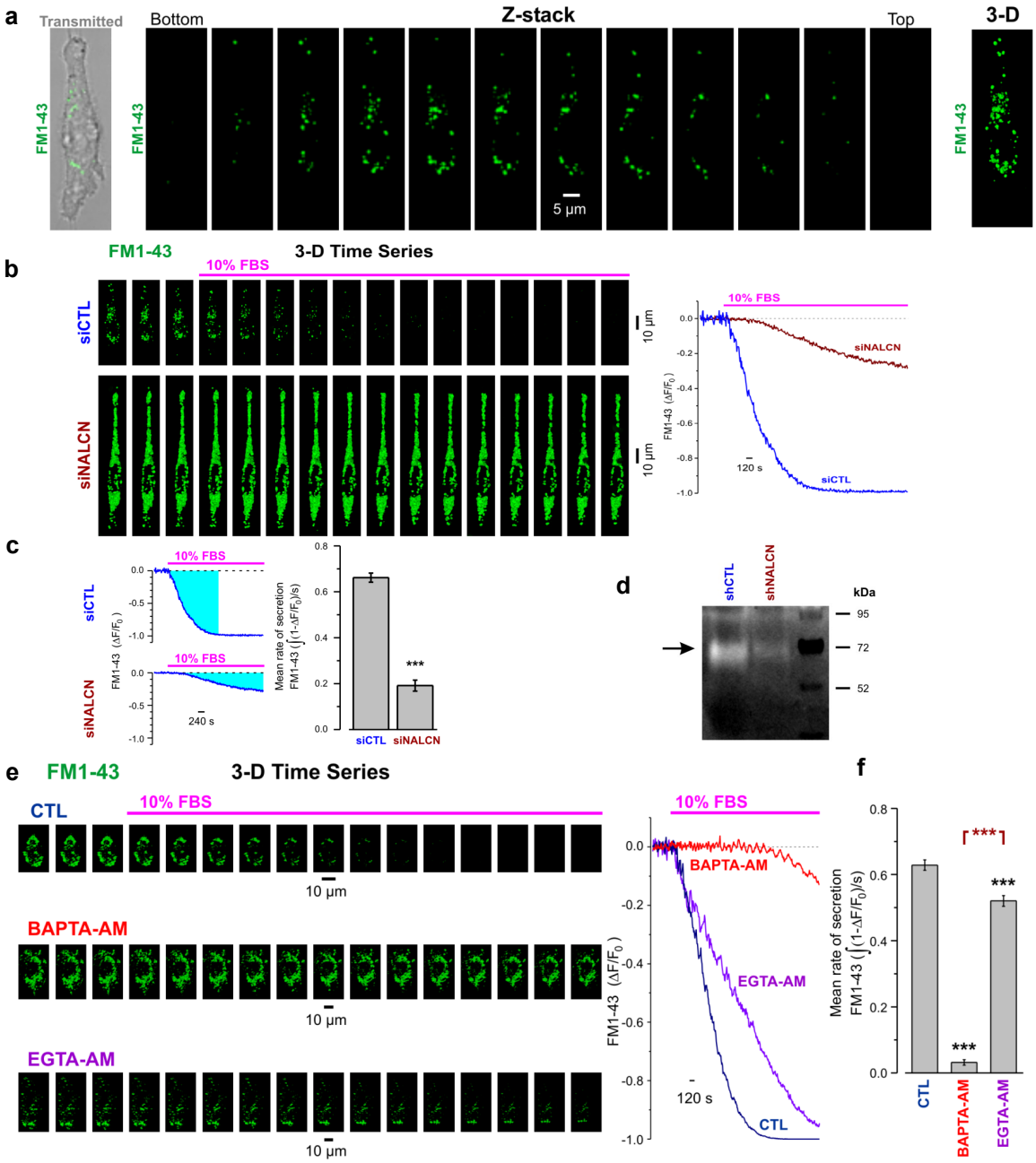

Figure 6. NALCN Regulates Vesicular Secretion of ECM-Degrading Enzymes in Ca2+-Dependent Manner.

(a) 3-D distribution of FM1-43-labelled secretory vesicles in PC-3 cell. Left: overlay of transmitted and x-y confocal images of FM1-43 fluorescence. Middle: confocal z-sections. Right: corresponding 3-D image. (b) Left: the galleries of sequential 3-D images (every 25th image) compare FBS-induced degradation of FM1-43-labelled secretory vesicles in PC-3 cells pre-treated with siCTL and siNALCN. Right: corresponding traces of relative changes in total z-stack fluorescence. (c) Plot compares mean rates of secretion, calculated as signal mass (cyan, left) per second, in control (siCTL: n=35) and following NALCN suppression (siNALCN: n=40). (d)

908 Zymography compares gelatinase activity (72 kDa) in shCTL and shNALCN. (e) The same as (b) but for
909 untreated (CTL) cells and those loaded with slow (EGTA-AM) and fast (BAPTA-AM) Ca2+ chelators. (f) The
910 same as (c) but compares the mean rates of secretion in CTL (n=45) and after treatment with EGTA-AM
911 (n=35) or BAPTA-AM (n=62). Data are mean±S.E.M. ***P<0.001, two-tailed Student's t-test.
912

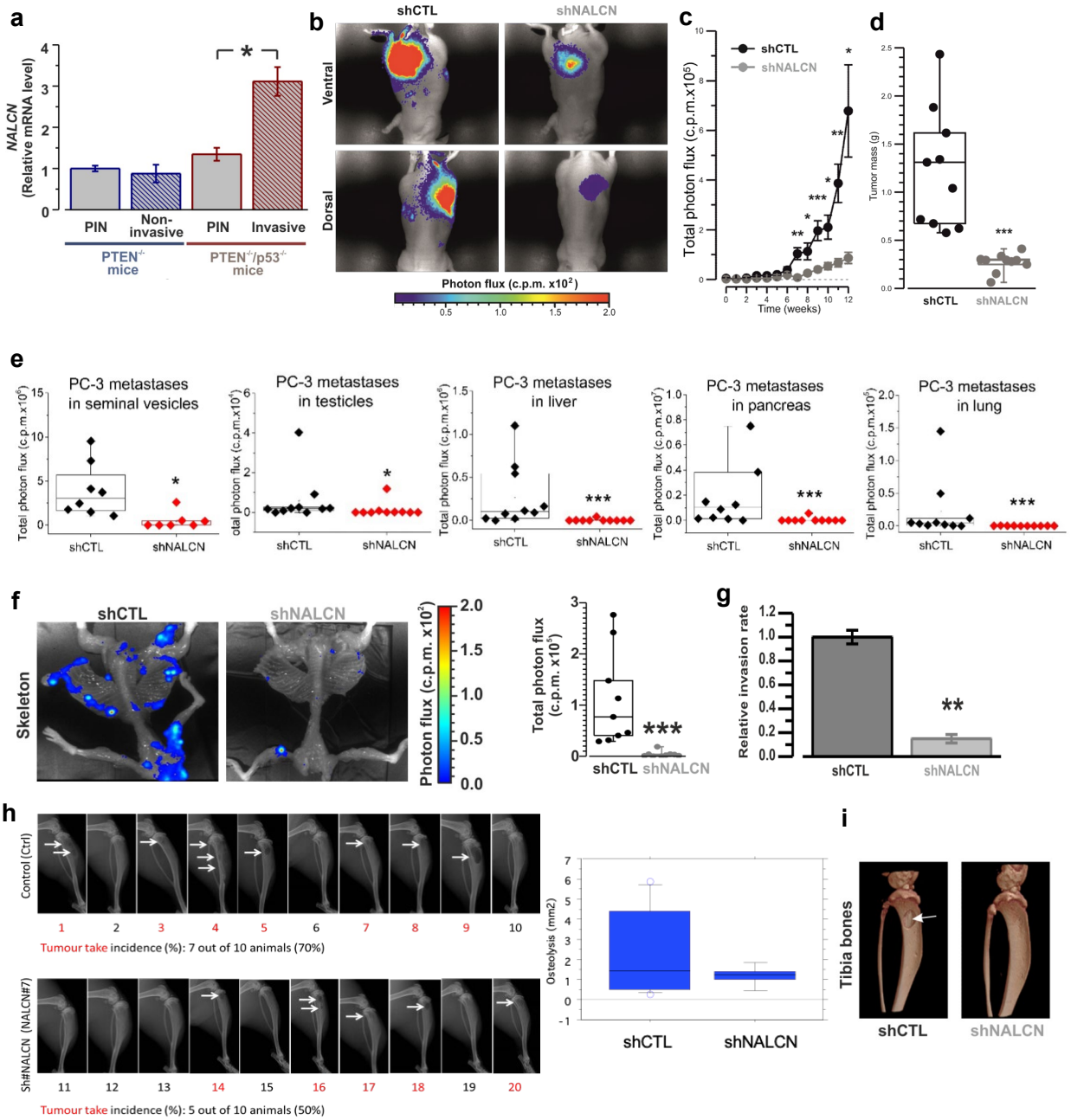

913

914 **Figure 7. In vivo and ex vivo analysis of NALCN tumorigenesis and metastatic spread.**
915 (a) NALCN mRNA level was not different between prostatic intraepithelial neoplasia (PIN) and non-invasive
916 prostate adenocarcinoma of PTEN(i)pe−/− mice. In contrast, invasive adenocarcinoma of PTEN/p53(i)pe−/−

mice exhibited significant upregulation of NALCN mRNA when compared with corresponding PIN. Data from PTEN(i)pe−/− mice were normalized to control PTEN(i)pe+/+ mice, whereas data from PTEN/p53(i)pe−/− mice - to control PTEN/p53(i)pe+/+ mice. RT-qPCR data are normalized to GAPDH and TBP and presented as mean±SEM (n=5). *P<0.05, two-tailed Mann-Whitney U test (b-c) Representative images (b) and analysis (c) of bioluminescence imaging (BLI) on mice after orthotopic injections of control (PC-3 Luc-shCTL) or NALCN knockdown cells (PC-3 Luc-shNALCN) revealed tumor growth suppression by NALCN knockdown (n=10). *P<0.05, **P<0.05, ***P<0.001, two-tailed Mann-Whitney U test. Counts per minute (c.p.m.). (d) Masses of tumors dissected from mice used in (c) 12 weeks after the injection: box-plots with raw data (n=10). ***P<0.001, two-tailed Mann-Whitney U test. (e) BLIs in mice organs. Counts per minute (c.p.m.). Box-plots with raw data from each mouse are shown. n.s. – non-significant, *P<0.05, ***P<0.001, two-tailed Mann-Whitney U test. (f) Ex vivo BLIs of skeleton metastases in mice 12 weeks after orthotopic injections of control (PC-3-Luc-shCTL) or NALCN depleted cells (PC-3-Luc-shNALCN). Right: box-plots with raw data of the BLI bone metastasis assay (n=10). ***P<0.001, two-tailed Mann-Whitney U test. (g) NALCN knockdown in PC-3 cells suppresses Transwell® (chemoattractant: conditioned media from osteoblasts) invasion from four independent experiments (n=4). Data are mean±S.E.M. **P<0.01, two-tailed Mann-Whitney U test. (h) X-ray images: osteolysis (arrow) 31 days after intra-tibial injection of control (PC-3 Luc-shCTL) or NALCN depleted cells (PC-3 Luc-shNALCN) with corresponding area (right) of osteolysis (mm2). Data: mean±S.E.M. (i) X-ray 3D images: osteolysis (arrow) 31 days after intra-tibial injection of PC-3-Luc-shCTL or PC-3-Luc-shNALCN cells.

Additional table and figures legends

NALCN		-	+	++	*P*
ISUP group	1	*n* = 47	*n* = 25	*n* = 3	0.0003
	2	*n* = 39	*n* = 42	*n* = 10	
	3	*n* = 37	*n* = 73	*n* = 17	
	4	*n* = 10	*n* = 9	*n* = 0	
Stage	pT2	*n* = 97	*n* = 93	*n* = 10	0.0003
	pT3	*n* = 36	*n* = 56	*n* = 20	

939 **Table S1. NALCN expression in hormone naïve clinically localized cancer**

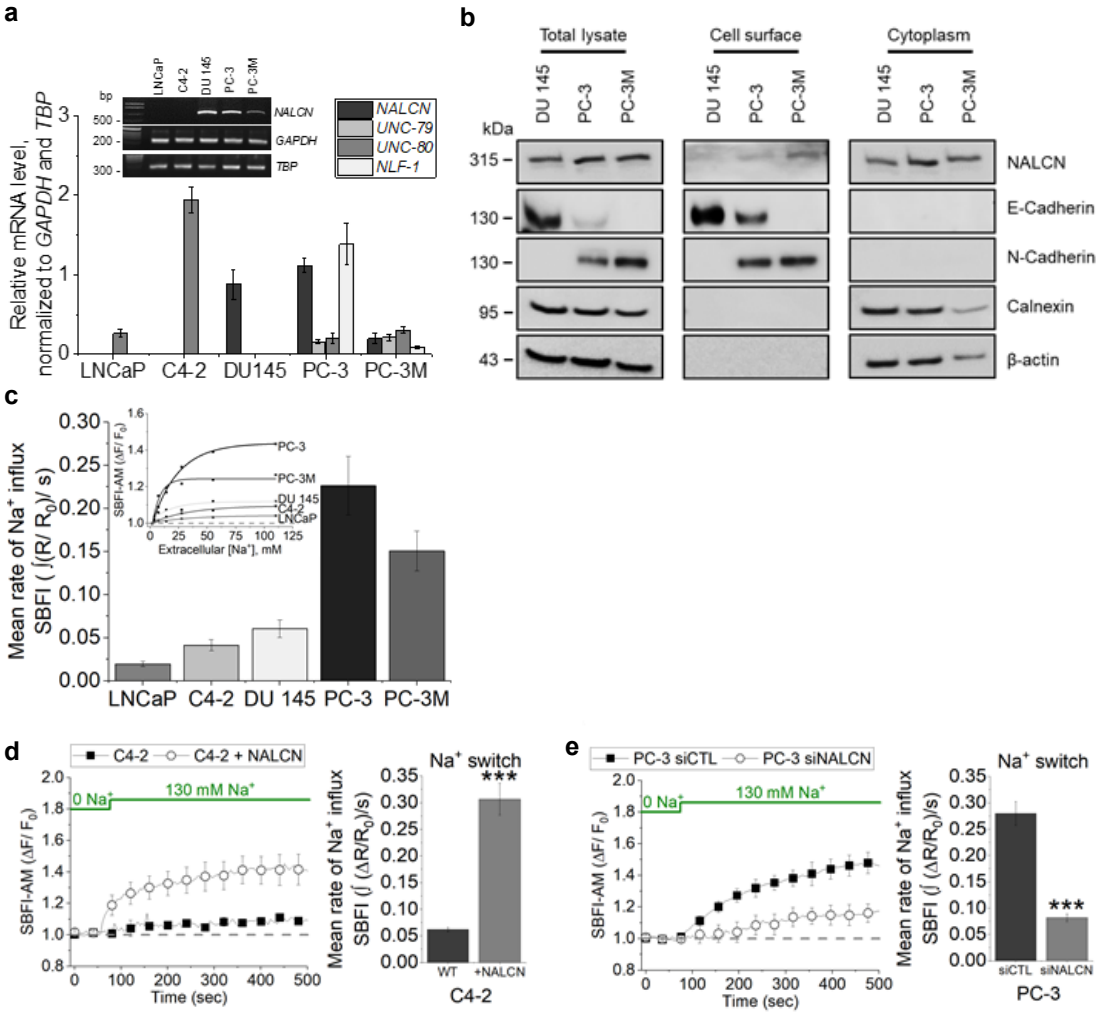

940

941 **Figure S1. Human prostate cancer cells express functional NALCN that mediates Na^+ influx**

942 (**a**) Conventional and RT-qPCR for NALCN channelosome genes in human prostate cancer (PCa) cell lines.
943 Data are normalised to GAPDH and TBP and are presented as mean values±SEM of five independent
944 experiments (n=5). (**b**) NALCN was found in plasma membrane biotinylated fraction of human prostate cancer
945 cells endogenously expressing the channel. E-Cadherin and N-Cadherin were used as plasmalemmal markers,
946 whereas calnexin and β-actin – as markers of cytoplasmic fraction. (**c**) Background Na^+ influx measured in
947 human prostate cancer cell lines using ratiometric dye SBFI-AM. The bar diagram plots: mean signal temporal
948 densities per cell (n=40-60). (**d**) In weakly metastatic C4-2 cells basal Na^+ influx was induced by transient
949 NALCN overexpression (+NALCN), when compared with wild-type cells (WT). The bar diagram plots: mean
950 signal temporal densities per cell (n=27-62). (**e**) In highly metastatic PC-3 cells transient NALCN silencing with

siRNA (siNALCN) resulted in suppression of basal Na+ influx, when compared with siRNA targeting firefly luciferase (siCTL). The bar diagram plots: mean signal temporal densities per cell (n=203-241). In (**d**) and (**e**) cells were transfected for 72 hours. Data are presented as mean values±SEM of three independent experiments. ***P<0.001, two-tailed Student's *t*-test.

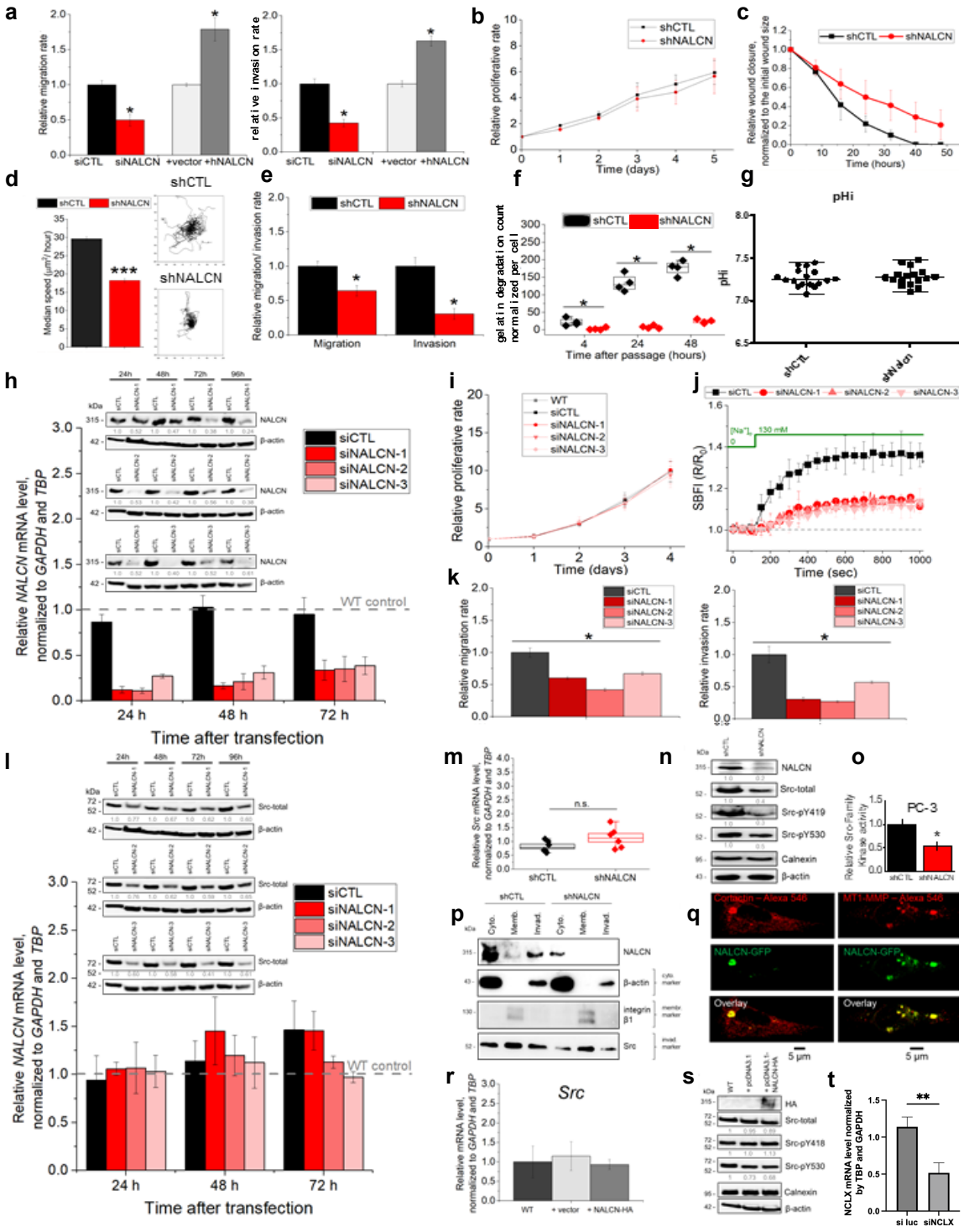

Figure S2. Role of NALCN in metastatic hallmarks of PC-3 cells

957 (**a**) Transwell® migration and Matrigel invasion assays after transient NALCN suppression and overexpression.
958 Control cells were transfected for 72 hours whether with siRNA targeting firefly luciferase (siCTL) or with an
959 empty vector pcDNA3.1 (+vector), whereas NALCN depleted cells – with siRNA-1 (siNALCN) and NALCN
960 overexpressing cells with pcDNA3.1-NALCN-HA (+NALCN). Data are presented as mean±S.E.M of four
961 independent experiments. *P<0.05, two-tailed Mann-Whitney U test. (**b**) Cellular proliferation assessed by
962 sulforhodamine B assay. (**c**) Wound-healing was slowed down in NALCN depleted cells. (**d**) Cellular motility
963 (calculated as μm2/hour) was remarkably inhibited in NALCN suppressed cells. Data are mean±S.E.M (n=838-
964 1629). ***P<0.001, two-tailed Student's t-test. Motility traces of individual control (shCTL) and NALCN
965 downregulated (shNALCN) cells (n=30). (**e**) Transwell® migration and Matrigel invasion assays for cells with
966 stable NALCN downregulation. Data are mean±S.E.M of four independent experiments. *P<0.05, two-tailed
967 Mann-Whitney U test. (**f**) Count of gelatin degradation dots produced by control (shCTL) and stable NALCN
968 knockdown (shNALCN) cells. Box-plots with raw data from four independent experiments are shown (n=4).
969 *P<0.05, two-tailed Mann-Whitney U test. (**g**) Intracellular pH was not affected by NALCN knockdown (n=17).
970 (**h**) NALCN mRNA and protein levels in non-transfected (WT control) cells and after transfection with siRNA
971 targeting firefly luciferase (siCTL) or transient NALCN silencing with siRNA-1 (siNALCN-1), siRNA-2 (siNALCN-
972 2), and siRNA-3 (siNALCN-3). RT-qPCR data are normalised to GAPDH and TBP. Immunoblotting data are
973 normalised to β-actin. Regardless of siRNA applied transient NALCN silencing did not affect proliferation (**i**) of
974 PC-3 cells, while suppressing the basal Na+ influx (**j**). Na+ imaging data are mean values±S.E.M. of three
975 independent experiments per cell (n=203-241). (**k**) Transwell® migration and Matrigel invasion assays as in (**a**).
976 Data are mean±S.E.M of four independent experiments (n=4). *P<0.05, two-tailed Mann-Whitney U test. (**l**) Src
977 mRNA and protein levels after transfection with siRNA targeting firefly luciferase (siCTL) or transient NALCN
978 silencing with siRNA-1 (siNALCN-1), siRNA-2 (siNALCN-2), and siRNA-3 (siNALCN-3). Src total– total protein
979 level, Src-pY419 – active form of Src, Src-pY530 – nonactive form of Src. RT-qPCR data are normalised to
980 GAPDH and TBP. Immunoblotting data are normalised to β-actin. (**m**) RT-qPCR for Src in control (shCTL) and
981 cells with stable NALCN suppression (shNALCN). Data are normalised to GAPDH and TBP and are presented
982 as mean±SEM of six independent experiments (n=6). n.s. – non-significant. (**n**) Representative immunoblot with
983 band intensities calculated for Src protein level as in (**m**). Data are normalised to β-actin and calnexin. (**o**) Kinase
984 activity assessed with ProFluor® Src-Family kinase assay. Data are mean values±S.E.M of four independent
985 experiments (n=4). *P<0.05, two-tailed Mann-Whitney U test. (**p**) Representative immunoblot of NALCN
986 localisation in cytoplasmic, membrane and invadopodial fractions after stable NALCN knockdown. (**q**)

987 Representative confocal images of co-localisation between green fluorescent protein (GFP)-tagged NALCN and
988 invadopodial markers: cortactin and MT1-MMP. (**r**) RT-qPCR for Src after transient overexpression of
989 haemagglutinin (HA)-tagged NALCN (+NALCN-HA). Data are normalised to GAPDH and TBP. (**s**)
990 Representative immunoblots with band intensities obtained for Src protein level as in (**r**). Data are normalised
991 to β-actin and calnexin. (**t**) RT-qPCR for NCLX in control (siLuc) and cells transfected by siNCLX . In (**b**), (**c**),
992 (**h**), (**i**), (**l**), (**n**), (**r**), (**s**) and (**t**) data are presented as mean values±S.E.M of three independent experiments.

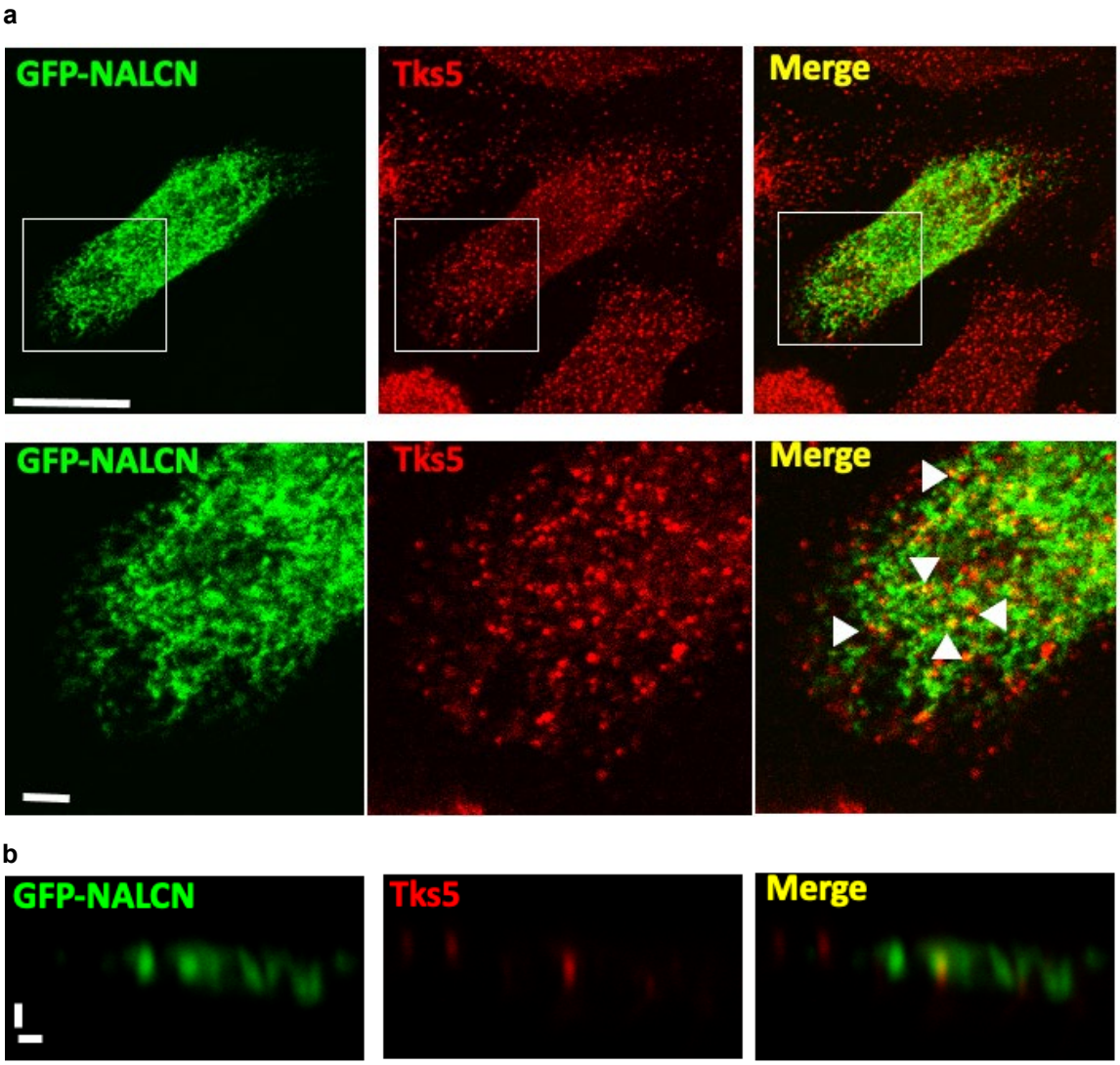

993

994 **Figure S3. Invadosome formation on gelatin layer**

995 (**a**) Confocal microscopy images of PC3 cells plated on gelatin and transfected with NALCN GFP, treated with
996 10% FBS in RPM1 overnight, and stained for endogenous Tks5 (in red) to visualize invadosomes. Scale bar,
997 15 μm. Lower inset panels highlight the colocalization of NALCN and Tks5. Scale bar, 1 μm. (**b**) Confocal
998 microscopy XZ section of PC3 cells plated on gelatin and transfected with NALCN GFP treated with 10% RPM1

overnight and stained for endogenous Tks5 (in red) to visualize invadosomes. Scale bar, 1 μm.

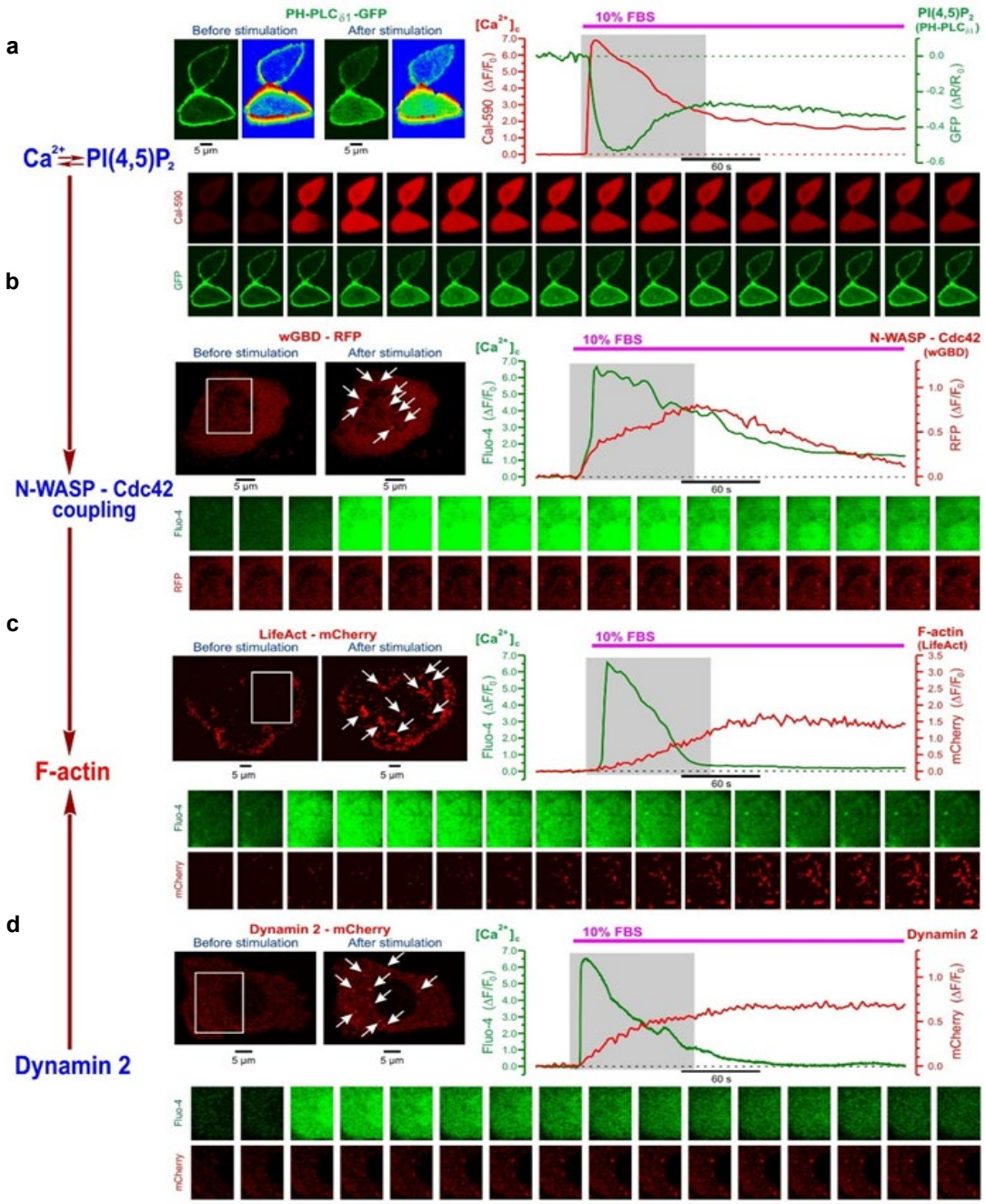

Figure S4. FBS-induced [Ca^{2+}]c response in PC-3 cells is associated with changes in PI(4,5)P2, N-WASP/Cdc42, dynamin and actin consistent with initiation of invadopodia formation

(**a**) Left: confocal images of PH-PLC$_{\partial 1}$ - GFP fluorescence captured before and 1 min after stimulation with 10% FBS, and their rainbow-coded 3D shaded-surface plots. Right: corresponding traces of relative (R=Fplasmalemma /Fcytosol) changes in GFP fluorescence (green), reflecting translocation PH-PLC$_{\partial 1}$ from the plasma membrane to cytosol caused by PI(4,5)P2 degradation, and in Cal-590 fluorescence (red) reflecting

1007 [Ca^{2+}]c dynamics. (**b**) Left: near cell bottom confocal (< 0.8 μm) images of wGBD - RFP fluorescence before
1008 and 2 min after stimulation with 10% FBS. Note puncta formation (arrows) reflecting spots where Cdc42 is
1009 activated to bind N-WASP. Right: corresponding traces of relative changes in RFP fluorescence (red), reflecting
1010 the dynamics of Cdc42 activation, and in Fluo-4 fluorescence (green) reflecting [Ca^{2+}]c dynamics. (**c**) Left: near
1011 cell bottom confocal (< 0.8 μm) images of PC-3 cell transfected with F-actin marker LifeAct - mCherry were
1012 captured before and 3 min after stimulation with 10% FBS. Note F-actin-enriched structures (arrows) induced
1013 by stimulation with FBS. Right: corresponding traces of relative changes in mCherry fluorescence (red),
1014 reflecting F-actin dynamics, and in Fluo-4 fluorescence (green) reflecting [Ca^{2+}]c dynamics. (**d**) Left: near cell
1015 bottom confocal (< 0.8 μm) images of PC-3 cell transfected with Dynamin 2 - mCherry were captured before
1016 and 2 min after stimulation with 10% FBS. Note dynamin puncta (arrows) induced by stimulation with FBS.
1017 Right: corresponding traces of relative changes in mCherry fluorescence (red) reflecting the dynamics of the
1018 dynamin puncta formation and in Fluo-4 fluorescence (green) reflecting [Ca^{2+}]c dynamics. The galleries below
1019 the plots show images (**a**) or enlarged boxed regions of the images (**b-d**) captured during the periods highlighted
1020 on the plots by grey background: every 3rd image (**a-c**), every 35th image (**d**).

1021

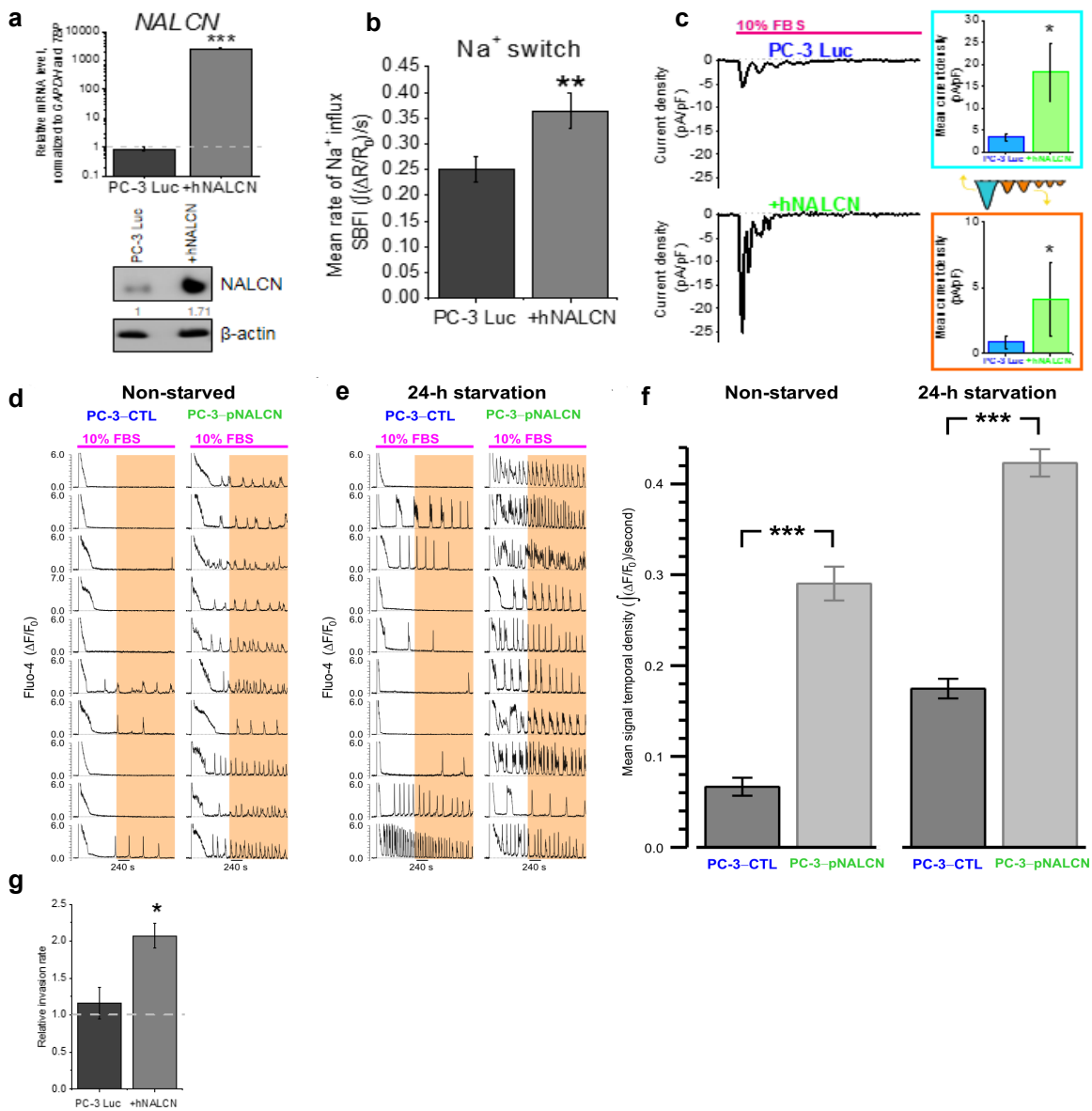

Figure S5. NALCN overexpression promotes metastatic cell behaviors in vitro and in vivo.

(**a**) NALCN mRNA and protein levels in control human prostate cancer cells permanently overexpressing luciferase (PC-3 Luc) and in cells stably overexpressing NALCN (+hNALCN). RT-qPCR data are normalised to GAPDH and TBP and are presented as mean values±S.E.M of three independent experiments (n=3); and related to mRNA level of PC-3 stably overexpressing mCherry (grey dashed line). ***P<0.001, two-tailed Mann-Whitney U test. Immunoblotting data are normalised to β-actin and are presented as mean of three independent experiments (n=3). (**b**) Mean rate of Na^+ (SBFI) influx calculated as signal mass (∫(ΔR/R0)/s) in PC-3 Luc and +hNALCN cells. The bar diagram plots: mean signal temporal densities per cell (n=141-287). Data are presented as mean ±S.E.M. of three independent experiments. **P<0.01, two-tailed Student's t-test. (**c**) Representative traces of the inward Na^+ current recorded using perforated patch-clamp technique. The FBS-

1033 induced inward Na^+ current in PC-3 was significantly larger in cells stably overexpressing NALCN than in control
1034 cells. The bar diagram plots: mean current densities (pA/pF; mean±S.E.M.) per cell (n=4-6) during initial
1035 transient (cyan) and oscillations (orange). *P<0.05, two-tailed Mann-Whitney U test. (**d**) and (**e**) Representative
1036 traces of FBS-induced $[Ca^{2+}]c$ responses reported by confocal time-series imaging of fluo-4 fluorescence.
1037 Overexpression of NALCN facilitates $[Ca^{2+}]c$ oscillations in non-starved and pre-starved PC-3 cells. (**f**) Mean
1038 signal (Fluo-4) temporal densities during highlighted periods were compared between PC-3 Luc and +hNALCN
1039 in non-starved (n=259 and n=254, respectively) and pre-starved (n=360 and n=317, respectively) cells. Data
1040 are mean values±S.E.M. ***P<0.001, two-tailed Student's *t*-test. (**g**) NALCN overexpression significantly
1041 increases invasiveness of PC-3 cells as reported by Transwell® Matrigel invasion assay. Data are presented
1042 as mean±S.E.M of four independent experiments and related to invasion rate of PC-3 stably overexpressing
1043 mCherry (grey dashed line). *P<0.05, two-tailed Mann-Whitney U test.

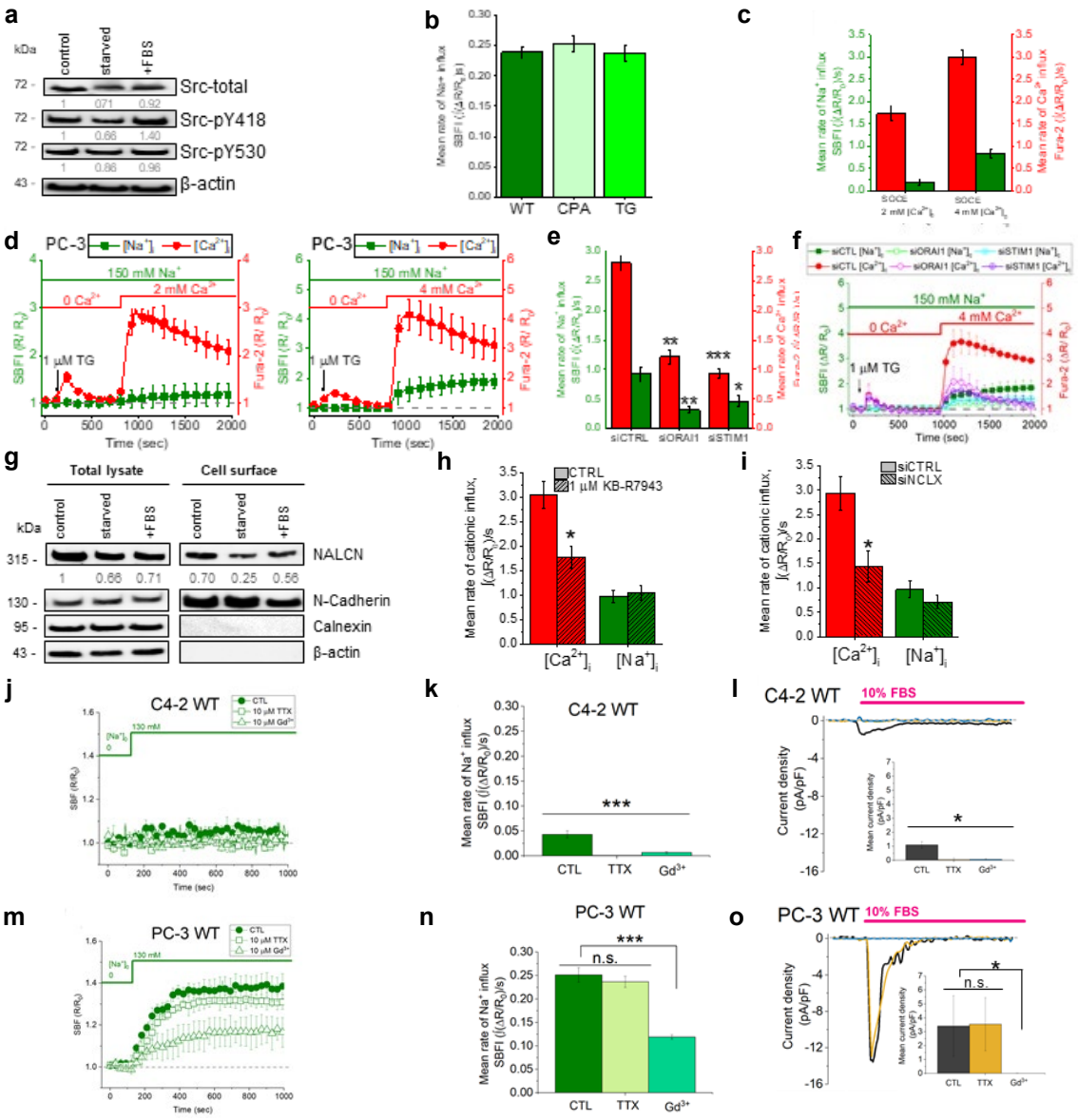

Figure S6. Interplay between store-operated Ca^{2+} entry (SOCE) and NALCN in PC3 cells

(**a**) Representative immunoblot with band intensities calculated for Src protein level in control, 24 h prestarved cells and FBS-stimulated cells after starvation (+FBS). Src total– total protein level, Src-pY419 – active form of Src, Src-pY530 – nonactive form of Src. Data are normalised to β-actin and are presented as mean values of three independent experiments (n=3). (**b**) Mean rate of Na^+ influx calculated as SBFI-AM signal mass (∫(ΔR/R0)/s) at different concentrations of extracellular Ca^{2+} ([Ca^{2+}]o) and after ER depletion with 50 μM cyclopiazonic acid (CPA) and 1 μM thapsigargin (TG). The bar diagram plots: mean signal temporal densities per cell (n=45-360). (**c**) Mean rate of Na^+ (SBFI) and Ca^{2+} (Fura-2) influx calculated as signal mass (∫(ΔR/R0)/s) during different SOCE components. The bar diagram plots: mean signal temporal densities per cell (n=283-360). (**d**) SOCE-induced changes of cytosolic concentrations of Na^+ ([Na^+]c, SBFI) and Ca^{2+} ([Ca^{2+}]c, Fura-2)

using 2 mM $[Ca^{2+}]o$ and 4 mM $[Ca^{2+}]o$. (**e**) and (**f**) SOCE-induced changes of $[Na^{+}]c$ (SBFI) and $[Ca^{2+}]c$ (Fura-2) in cells transfected for 48 hours with siRNA targeting firefly luciferase (siCTL), ORAI1 (siORAI1) and STIM1 (siSTIM1). Mean rate of Na^{+} (SBFI) and Ca^{2+} (Fura-2) influx calculated as signal mass (∫(ΔR/R0)/s) after silencing of major SOCE players. The bar diagram plots: mean signal temporal densities per cell (n=109-182). *P<0.05, **P<0.01, ***P<0.001, two-tailed Student's t-test. (**g**) Representative immunoblot with band intensities calculated for NALCN protein level in total cell lysate and biotinylated plasma membrane fraction. N-Cadherin was used as plasmalemmal marker, whereas ER-residing protein calnexin and cytoskeletal β-actin – as markers of cytoplasmic fraction. For cytoplasmic fraction data are normalised to β-actin and calnexin, whereas for plasmalemmal fraction data are normalised to N-Cadherin, all data are presented as mean values of three independent experiments (n=3). (**h**) and (**i**) Mean rate of Na^{+} (SBFI) and Ca^{2+} (Fura-2) influx calculated as signal mass (∫(ΔR/R0)/s) after pharmacological inhibition of NCX-reverse mode (1 μM KB-R7943) (h) and mitochondrial NCLX silencing (siNCLX) (**i**). The bar diagram plots: mean signal temporal densities per cell (n=134-289). *P<0.05, two-tailed Student's *t*-test. (**j**) and (**m**) Background Na^{+} influx measured using ratiometric dye SBFI-AM in NALCN-negative human prostate cancer cell line, C4-2 WT, and endogenously expressing NALCN human prostate cancer cell line, PC-3 WT. In the latter, Na^{+} influx is tetrodotoxin (TTX)-resistant and gadolinium (Gd3+)-sensitive, as previously described for NALCN-mediated current (INALCN) in neurons. (**k**) and (**n**) The bar diagram plots: mean signal temporal densities per cell (for C4-2, n=702-772; for PC-3, n=1117-1571). Data are presented as mean ±S.E.M. of six independent experiments. n.s. – non-significant, ***P<0.001, two-tailed Student's *t*-test. (**i**) and (**o**) Representative traces of the inward Na^{+} current recorded using perforated patch-clamp technique. In C4-2 cell line, TTX or Gd^{3+} applications both completely abolished relatively small FBS-induced inward Na^{+} current. In contrast, the FBS-induced inward Na^{+} current in PC-3 cells was significantly larger, resistant to TTX but sensitive to Gd^{3+}. The bar diagram plots: mean current densities (pA/pF; mean±S.E.M.) per cell (n=4-6). n.s. – non-significant, *P<0.05, two-tailed Mann-Whitney U test.

In (**b**), (**c**), (**d**), (**f**), (**i**) and (**j**) data are presented as mean values±SEM of three independent experiments.

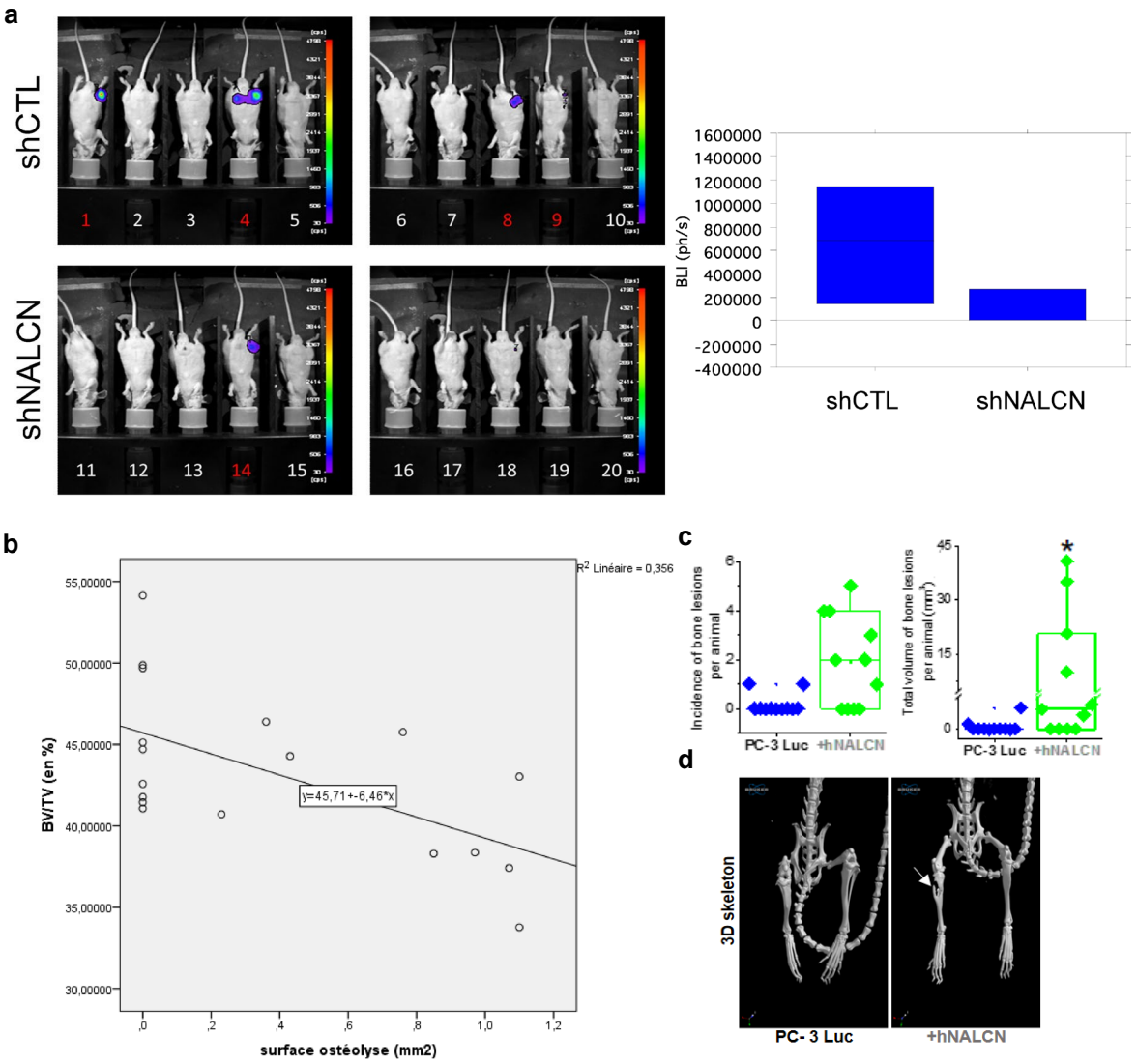

Figure S7. Analysis of bone tissue destruction

(**a**) Bioluminescence of mice 31 days after intra-tibial injection of control (PC-3 Luc-shCTL) or NALCN depleted cells (PC-3 Luc-shNALCN) with corresponding signal analysis (photons/s). Data are mean±S.E.M. (**b**) Correlation between osteolysis surface (mm^2) and bone volume/total volume (BV/TV, %). P =0,009. two-tailed Mann-Whitney U test. (**c**) Incidence and total volume of bone lesions in mice 8 weeks after intracardiac injections with control (PC-3 Luc) and cells stably overexpressing NALCN (+hNALCN). Box-plots with raw data from each mouse are shown. *P<0.05, two-tailed Mann-Whitney U test. (**d**) 3D illustrations of representative skeletal lesions.

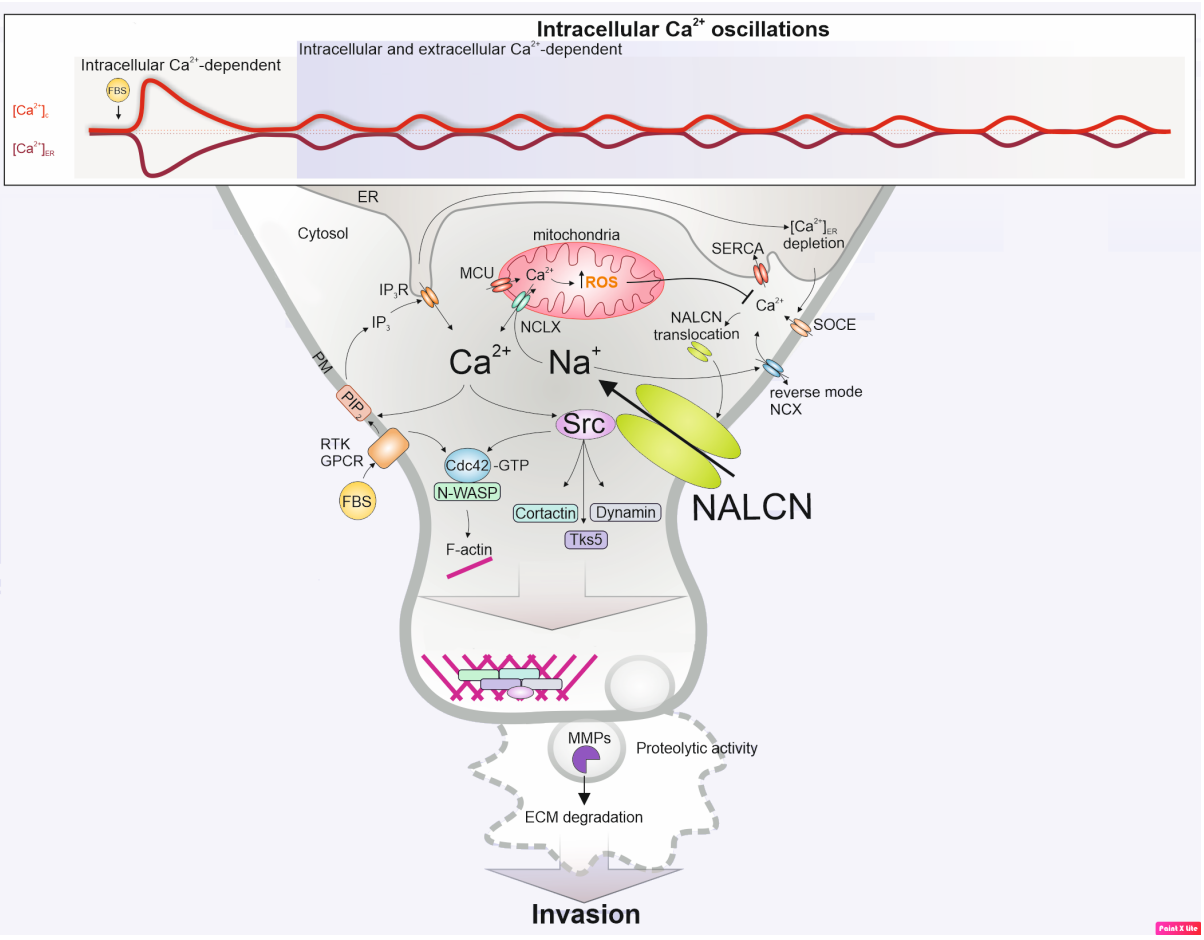

Figure S8. Schematic representation of signaling pathways employed by NALCN to promote cancer cell invasiveness.

Abbreviations: PM – plasma membrane, ER – endoplasmic reticulum, NALCN – Na^+ leak channel non-selective, RM-NCX – reverse mode of Na^+/ Ca^{2+} exchanger, NCLX – mitochondrial Na^+/ Ca^{2+} exchanger, IP3R – inositol 1,4,5-trisphosphate receptor, SERCA –sarco/endoplasmic reticulum Ca^{2+}-ATPase, MCU – mitochondrial Ca^{2+} uniporter, RTK – receptor tyrosine kinases, GPCR – G-protein coupled receptors, Src – proto-oncogene Src tyrosine kinase, N-WASP – neural Wiskott-Aldrich syndrome protein, ECM – extracellular matrix, MMPs – matrix metalloproteinases, GTP – guanosine-5'-triphosphate, ROS – reactive oxygen species, $[Ca^{2+}]c$ – cytosolic Ca^{2+} concentration, $[Ca^{2+}]ER$ – Ca^{2+} concentration in ER, $[Ca^{2+}]mito$ – Ca^{2+} concentration in mitochondria, $[Na^+]c$ – cytosolic Na^+ concentration, [ROS]mito – ROS concentration in mitochondria.

Briefly: (i) IP3R-mediated Ca^{2+} release caused by FBS-induced activation of RTK/GPCR causes the ER Ca^{2+} depletion and SOCE; elevation of $[Ca^{2+}]c$ in sub-PM microdomains facilitates NALCN translocation to PM and Na^+ influx promoting RM-NCX and additional Ca^{2+} influx; this triggers SERCA-mediated Ca^{2+} uptake into the ER and MCU-mediated Ca^{2+} uptake into mitochondria; the latter facilitates production of ROS, known to inhibit SERCA, RM-NCX and SOCE elements, and is opposed by NCLX exchanging Na^+, delivered by NALCN, to

1104 mitochondrial Ca^{2+}; these positive and negative feedbacks give rise to $[Ca^{2+}]c$ oscillations maintaining the
1105 activity Src, known as essential component of NALCN channelosome; active Src phosphorylates downstream
1106 proteins (cortactin, dynamin and Tks5) recruiting them to actin polymerization regions and giving rise to
1107 “invadopodia puncta”. (ii) RTK/GPCR activation is linked to activation of the Rho family GTPase, Cdc42, leading
1108 to its binding with N-WASP and subsequent actin nucleation. (iii) Invadopodia maturation is facilitated by Ca^{2+}-
1109 dependent secretion of MMPs degrading ECM.